

ARTIFICIAL MUSCLES

Sheath-run artificial muscles

Jiuke Mu¹, Mônica Jung de Andrade¹, Shaoli Fang¹, Xuemin Wang^{2,3}, Enlai Gao^{1,4}, Na Li^{1,5}, Shi Hyeong Kim¹, Hongzhi Wang⁶, Chengyi Hou⁶, Qinghong Zhang⁶, Meifang Zhu⁶, Dong Qian², Hongbing Lu², Dharshika Kongahage⁷, Sepehr Talebian⁷, Javad Foroughi⁷, Geoffrey Spinks⁷, Hyun Kim⁸, Taylor H. Ware⁸, Hyeon Jun Sim⁹, Dong Yeop Lee⁹, Yongwoo Jang⁹, Seon Jeong Kim⁹, Ray H. Baughman^{1*}

Although guest-filled carbon nanotube yarns provide record performance as torsional and tensile artificial muscles, they are expensive, and only part of the muscle effectively contributes to actuation. We describe a muscle type that provides higher performance, in which the guest that drives actuation is a sheath on a twisted or coiled core that can be an inexpensive yarn. This change from guest-filled to sheath-run artificial muscles increases the maximum work capacity by factors of 1.70 to 2.15 for tensile muscles driven electrothermally or by vapor absorption. A sheath-run electrochemical muscle generates 1.98 watts per gram of average contractile power—40 times that for human muscle and 9.0 times that of the highest power alternative electrochemical muscle. Theory predicts the observed performance advantages of sheath-run muscles.

Remarkable performance has been obtained for tensile and torsional carbon nanotube (CNT) hybrid yarn muscles (1–5), whose actuation is driven by the volume change of a guest within a twisted or coiled CNT yarn. During thermally powered contraction, coiled hybrid muscles can deliver 29 times the work as the same weight human muscle (1). Changing the structural relationship between guest and host will provide major performance increases and the ability to replace expensive CNT yarn with cheap commercialized yarns.

CNT hybrid yarn artificial muscles (HYAMs) can be made by inserting twist, or twist and coiling, into a guest-filled CNT yarn. Muscles that are twisted (but not coiled), called twisted muscles, are mainly useful for torsional actuation. High inserted twist results in coiled muscles that can deliver larger strokes than can human muscles (1).

Polymer fiber and yarn muscles are known (6–11) that operate similarly to CNT HYAMs: Muscle volume expansion drives muscle untwist, which produces both torsional and tensile actuation. These thermally driven polymer muscles are cheap because they can be made by inserting

extreme twist into fishing line or sewing thread. Other twisted or coiled materials have been exploited as fiber-like muscles, such as graphene oxide fiber (12), shape memory polymer fiber or metal alloy yarn (13, 14), cotton yarn composites (15), carbon fiber/polydimethylsiloxane yarn (16), neat CNT yarns (1, 17–20), and spider-silk dragline (21). CNT HYAMs are especially useful because guest choice results in muscles driven thermally (1, 4), electrochemically (22, 23), or by absorption (2, 3, 24).

The challenge is to develop a fundamentally new host-guest structure that eliminates the liabilities of CNT HYAMs. First, the ability of guest expansion to drive yarn untwist depends on the yarn's bias angle (the angle between the yarn length and the nanotube direction). Because this angle decreases to zero on going from the yarn surface to the yarn center, the input energy delivered to the guest near the yarn center is not effectively used. Second, muscle mechanical power is limited by the chemical or thermal transport times to access yarn volume.

Here, we describe a new muscle structure that addresses each of these problems. Rather than infiltrating a volume-changing yarn guest within a yarn, such as for a HYAM, this guest is coated as a yarn sheath. Because the dimensional and modulus changes of this sheath drive actuation, we call the resulting actuators “sheath-run artificial muscles” (SRAMs).

CNTs were drawn as a sheet from a CNT forest and twisted into the Archimedian yarn (fig. S1) (25, 26) used as muscle core. SRAMs were fabricated (Fig. 1A) by drawing a vertically suspended, torsionally tethered twisted yarn through a large droplet of polymer solution multiple times to achieve the targetted sheath thickness of dried polymer. The solvent used was chosen to avoid polymer infiltration into the twist-densified core yarn and provide a sharp interface between sheath and core (Fig. 1C and figs. S2A, S3, and S7, C to F). Scanning electron microscope (SEM) measurements provided the sheath/core ratio

(SCR; the ratio of sheath thickness to the interior yarn diameter). To demonstrate that CNT yarns can be replaced with inexpensive yarns, we evaluated commercial nylon 6, silk, and bamboo yarns as the muscle core as well as electrospun polyacrylonitrile (PAN) nanofibers.

The nomenclature used for a sheath X on a yarn core Y of a SRAM or an X guest inside a HYAM yarn Y is $X@Y$. Hence, PEO-SO₃@CNT denotes a PEO-SO₃ guest and a CNT yarn host, where PEO-SO₃ is a blend of poly(ethylene oxide) and a copolymer of tetrafluoroethylene and sulfonyl fluoride vinyl ether (26). The yarn-bias-angle dependence of the minimum SCR needed to prevent sheath cracking for a PEO-SO₃@CNT yarn is shown in fig. S7; this ratio approximately maximizes torsional stroke for the high targeted yarn bias angle. For comparative studies, the guest/host weight ratio was essentially the same for the SRAM and HYAM, and the same mechanical load was applied during twist insertion. HYAMs were made by using the above droplet method by adding polymer solution to a low-twist yarn, partially drying the solution to a gel-like state and then adding additional twist to equal that of the SRAM. If the guest/host weight ratio is too high for a HYAM (26), the guest will extrude from the host yarn during twist insertion (fig. S12B).

“Self-coiled” yarn was fabricated by inserting further twist while the guest was in the gel state (Fig. 1B). To increase yarn stroke by increasing the spring index, twisted yarns or self-coiled yarns (Fig. 1, D and E) were coiled or supercoiled by wrapping around a mandrel. Afterward, the coiled yarn was thermally annealed (26). When describing a muscle, the diameter is for the dry, twisted muscle before coiling. Unless otherwise described, gravimetric work and power densities are normalized to the weight of the dry muscle. The spring index is the ratio of the difference in outer coil diameter and the fiber diameter to the fiber diameter, where a fiber's diameter is its width in its largest lateral dimension.

Torsional actuation of a one-end-tethered SRAM is illustrated in Fig. 2A. Unless otherwise noted, an equilibrium vapor pressure was delivered to muscles in flowing dry air and then removed under vacuum, using the glass tube system of Fig. 2B. For performance comparisons, a 60-mg-weight paddle at the yarn end, with 0.28 kg·mm² moment of inertia, was used to characterize torsional rotation angle and speed. Also, the SRAMs and HYAMs were made from identical yarn, contained the same inserted twist, and had nearly the same host/guest weight ratio.

In Fig. 2B, we compare the time dependence of paddle rotation and speed for a PEO-SO₃@CNT SRAM and HYAM and a pristine CNT muscle that are undergoing one complete reversible cycle of ethanol vapor-powered actuation. The peak stroke and peak rotation speed for the SRAM [143°/mm and 507 rotations per minute (rpm)] are about twice that for the HYAM (76°/mm and 254 rpm) and much larger than for the pristine yarn (4.7°/mm and 36 rpm). Steady-state measurements of torsional stroke versus weight % (wt %) ethanol in the muscles (Fig. 2C) show that

¹Alan G. MacDiarmid NanoTech Institute, The University of Texas at Dallas, Richardson, TX 75080, USA. ²Department of Mechanical Engineering, The University of Texas at Dallas, Richardson, TX 75080, USA. ³Department of Mechanical Engineering, Georgia Southern University, Statesboro, GA 30458, USA. ⁴Department of Engineering Mechanics, School of Civil Engineering, Wuhan University, Wuhan, Hubei 430072, China. ⁵Materials Science, MilliporeSigma, Milwaukee, WI 53209, USA. ⁶State Key Laboratory for Modification of Chemical Fibers and Polymer Materials, College of Material Science and Engineering, Donghua University, Shanghai 201620, China. ⁷Intelligent Polymer Research Institute, Australian Institute for Innovative Materials, University of Wollongong, Wollongong, New South Wales 2522, Australia. ⁸Department of Bioengineering, The University of Texas at Dallas, Richardson, TX 75080, USA. ⁹Center for Self-Powered Actuation, Department of Biomedical Engineering, Hanyang University, Seoul 04763, South Korea.

*Corresponding author. Email: ray.baughman@utdallas.edu

the ratio of torsional strokes for a PEO-SO₃@CNT SRAM to a PEO-SO₃@CNT HYAM peaks at 6.7 for 4.1 wt % ethanol and then gradually decreases to 1.7 for 17.5 wt % ethanol. The small hysteresis in torsional strokes for the SRAM and HYAM means that both could reliably open and close valves in response to absorbed vapor. However, the torsional stroke of the SRAM is much more sensitive to the amount of absorbed ethanol than the HYAM.

As shown in Fig. 2D, PEO-SO₃@CNT SRAMs and HYAMs reversibly actuate over 3000 cycles of ethanol absorption and desorption, despite the absence of tethering. This reversibility results because the guest acts as a torsional return spring. By contrast, the torsional stroke of the pristine yarn rapidly decreases from 27°/mm for the first cycle to ~4.7°/mm on the 27th cycle, thereafter stabilizing at this value for the next ~3000 cycles.

Our theoretical model (26) predicts the dependence of torsional stroke on the SCR by using the torque balance between sheath and core, before and after actuation. This analysis captures the two primary mechanistic contributions to SRAM torsional actuation: sheath swelling and sheath softening, which combine to partially release elastically stored torsional energy in the core yarn. In Fig. 2E, we compare the observed and predicted dependence of torsional stroke on SCR for an ethanol-driven PEO-SO₃@CNT SRAM made from a 42°-bias-angle yarn. The maximum torsional stroke (143°/mm) occurs for a SCR of 0.14, which agrees with the predicted 151°/mm stroke maximum for a SCR of 0.15. A much lower SCR cannot maintain the initially inserted twist before actuation, and a much higher SCR ratio hinders twist release during actuation. As shown in fig. S6, the torsional stroke is near maximum for yarn bias angles from 38° to 43° for a PEO-SO₃@CNT SRAM that has a sheath/core weight ratio of 0.53.

Torsional stroke is sensitive to vapor type (fig. S8) and the sheath's ability to swell and soften by vapor absorption. Because ethanol produces a much larger equilibrium volume expansion in PEO-SO₃ (16.7%) than in polyvinyl alcohol (PVA) (1.3%) or nylon 6 (0.5%) (fig. S5A), the torsional stroke of a CNT core SRAM was much larger for a PEO-SO₃ sheath (143°/mm) than for PVA (22°/mm) or nylon 6 sheaths (11°/mm) (fig. S5B).

High performance resulted for ethanol-powered torsional SRAMs in which the expensive CNT yarn was replaced with a silk or electrospun PAN yarn (Fig. 2F and fig. S2B). The bias angles of these SRAMs (30° and 18°, respectively) are lower than for the CNT yarn core SRAM (42°) because higher twist broke the yarns. The lower bias angles and larger diameters of the PAN and silk core yarns provided smaller equilibrium torsional strokes (123 and 70°/mm, respectively) than for the PEO-SO₃@CNT SRAM (143°/mm). However, using the invariance of the product of torsional stroke and yarn diameter when the yarn's bias angle is constant (1) and results in fig. S6 for the bias-angle-dependence of torsional stroke for a PEO-SO₃@CNT SRAM, the torsional strokes of a PEO-SO₃@PAN SRAM and a PEO-SO₃@silk

SRAM are predicted to be close to those for PEO-SO₃@CNT SRAMs that have the same core bias angle and diameter (26).

All measurements show that a SRAM has important performance advantages over the corresponding HYAM as a torsional actuator. The ratios of peak torsional speed of the SRAM to that of the corresponding HYAM are nearly the same for PEO-SO₃@CNT (1.75), PEO-SO₃@silk (1.74), and PEO-SO₃@PAN (1.79) muscles powered by ethanol vapor and close to that for water vapor-powered nylon6@CNT muscles (1.86) (Fig. 2, B and F, and figs. S2 and S9). However, greater variation arises in the ratios of peak stroke for the SRAM to that of the HYAM (1.86, 1.67, 1.36, and 1.63, respectively, for the above).

By adding sufficient additional twist to the muscles used for torsional actuation, fully coiled yarn muscles result that provide large strokes. By comparing the performance of coiled muscles made from yarns with nearly the same host and guest weight per yarn length, we demonstrate the increases in stroke, stroke rate, contractile work, and contractile power that results from transitioning from a HYAM to a SRAM.

The torsional rotor was replaced with a heavy, nonrotating weight when changing from torsional to tensile actuation. Allowing weight rotation decreases tensile contraction (fig. S10) because yarn untwist increases muscle length. When ethanol vapor-driven, a PEO-SO₃@CNT SRAM delivered a higher stroke for all loads and times than did a HYAM (Fig. 3, A and B, and fig. S11). One thousand fully reversible cycles were demonstrated. Corresponding SRAM structure changes during 0.1 Hz actuation to provide 8.5% stroke are shown in movie S1. As shown in fig. S12A, the equilibrium isometric contractile

stress generated by a PEO-SO₃@CNT SRAM monotonically increases with increasing ethanol vapor concentration. By contrast, if the applied load is low and the change in sheath thickness is large, the SRAM first contracts until intercoil contact occurs and then expands as intercoil contact drives actuation (fig. S12C). Mandrel coiling greatly amplifies muscle stroke. A 70% tensile stroke was obtained for a humidity-driven cone-mandrel SRAM, and this SRAM provided faster contraction than that of cylindrical-mandrel SRAMs that were coiled and supercoiled (fig. S13).

The SRAMs provide advantages in contractile work capacity and maximum average contractile power (Fig. 3B, figs. S14 to 16 and S19, and table S2), which is the maximum ratio of contractile work to actuation time. The maximum average contractile power output was 4.44 W/g for the ethanol vapor-driven PEO-SO₃@CNT SRAM and 1.51 W/g for the corresponding HYAM. The load-optimized contractile work capacity and the maximum average power density of coiled SRAMs are higher than for coiled HYAMs at all applied loads for sorption-driven, electrothermal, and electrochemical actuation (table S2). For loads maximizing equilibrium contractile work capacities, the SRAM-to-HYAM work capacity ratio was 1.84 for ethanol vapor-driven PEO-SO₃@CNT muscles (Fig. 3B), 1.73 for electrothermally driven PEO-SO₃@CNT muscles (Fig. 3D), and 2.15 for electrothermally driven PU@CNT muscles (Fig. 4D), where PU is an elastomeric polyurethane (26). These SRAM-to-HYAM work capacity ratios will approximately equal the ratio of energy conversion efficiencies for sorption-powered muscles in which the equilibrium gravimetric sorption of guest in SRAM sheath and in HYAM core are equal, and for thermal muscles in which the

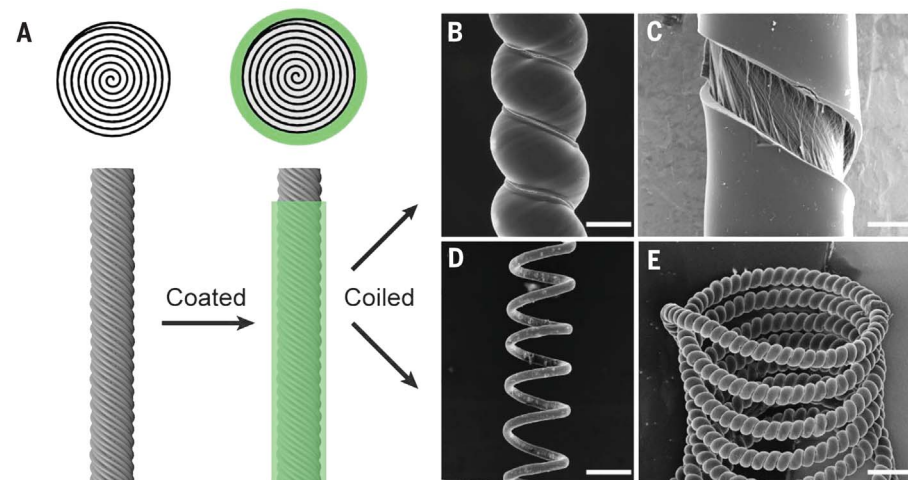


Fig. 1. Muscle fabrication and structure for torsional and tensile actuation. (A) Schematic lateral and cross-sectional views of a twisted CNT yarn and a SRAM, made by coating a twisted CNT yarn with a polymer sheath. (B to E) SEM micrographs for PEO-SO₃@CNT muscles. (B) A SRAM made by self-coiling a sheath-coated twisted yarn. (C) The surface of a twisted SRAM, which was broken by untwisting in liquid N₂, showing the distinct boundary between sheath polymer and CNT core. (D) A mandrel-coiled twisted SRAM. (E) A SRAM that was self-coiled and then supercoiled around a mandrel. Scale bars, (B) to (E), 35, 15, 200, and 200 μm, respectively.

differences in heat lost during high-rate contractile work are negligible.

The SRAM-to-HYAM power density ratio (table S2) is higher for ethanol vapor-driven PEO-SO₃@CNT muscles (2.94) than for electrothermally driven PEO-SO₃@CNT muscles (1.69) and PU@CNT muscles (2.06). This is likely because the power density ratio for the vapor-driven muscle is enhanced by both the larger

equilibrium work capacity of the SRAM and the more rapid vapor absorption, and the latter diffusion-based enhancement term disappears when actuation is from electrothermally heating the CNT yarn.

Because the rate of cooling is faster for the SRAM than for the HYAM and the rate of cooling has the greatest impact on full cycle performance, the high-frequency work capacity during

electrothermal actuation is much higher for a SRAM than a HYAM. The PEO-SO₃@CNT SRAMs electrothermally operated in air and in room-temperature water to produce 2.6 W/g (for 3.2% stroke at 9 Hz) and 9.0 W/g (for 5.5% stroke at 12 Hz), respectively, of full-cycle contractile power (fig. S15, C to F), which is much higher than the typical contractile power of human natural muscle (0.05 W/g, 5). When operated in air, this SRAM muscle provided a stroke of 8.0% at 2 Hz, corresponding to a power density of 1.2 W/g. Shown in movie S2 is the electrothermal actuation of a coiled PEO-SO₃@CNT SRAM in water at 12 Hz to generate a 5% stroke and a full-cycle contractile power of 4.2 W/g.

We next predicted the stress dependence of tensile stroke and contractile work capacity for ethanol-powered actuation of coiled PEO-SO₃@CNT SRAMs and HYAMs (fig. S21) (26). This analysis used the above theoretically derived torsional strokes of twisted, noncoiled muscles, the relationship between torsional stroke (ΔT) and tensile stroke for noncontacting coils if muscle stiffness were constant, and the dependence of PEO-SO₃ modulus on ethanol absorption (fig. S4A). Remarkable agreement was obtained between theory and experiment for the stress dependence of equilibrium stroke and contractile work capacity without using a fitted parameter. The observed ratio of the maximum contractile work capacity of the SRAM to that of the HYAM is 1.70, which is close to the predicted 1.52 (fig. S22).

Electrochemically powered artificial muscles have key advantages over thermally powered muscles: (i) Their efficiency is not limited by the Carnot efficiency, and (ii) they have a natural latching state, meaning that stroke can be maintained without the input of substantial electrical energy. A conventional electrochemical CNT yarn muscle is a HYAM, in which the yarn guest is the electrolyte.

A CNT@nylon6 SRAM was made with the process shown in Fig. 4A, right. Similar to a process used to make coiled CNT yarns for energy harvesting (27), a stack of CNT sheets was formed into a cylinder (Fig. 4A, left). A nylon yarn was placed in the center of the cylinder. Initially, twist is inserted only into the CNT cylinder. However, once the CNT cylinder collapses to form a sheath on the nylon 6 yarn, torque automatically transfers from this sheath to the yarn, enabling the yarn to become fully coiled.

The electrolyte-filled CNT sheath of the SRAM and the electrolyte-filled volume of the HYAM provide electrochemical actuation because of volume changes produced by electrochemical double-layer injection of anions and cations. For the used electrolyte of 0.2 M tetrabutylammonium hexafluorophosphate (TBA-PF₆) in propylene carbonate, the calculated van der Waals volume (28) of the TBA⁺ cation (~293 Å³) is much larger than for the PF₆⁻ anion (69 Å³). Potential scans (Fig. 4B) for the SRAM and HYAM show that muscle contractions increase on both sides of the potential of zero charge and that the contraction is proportional to the volume of the injected ion. These contractions are largest for the SRAM.

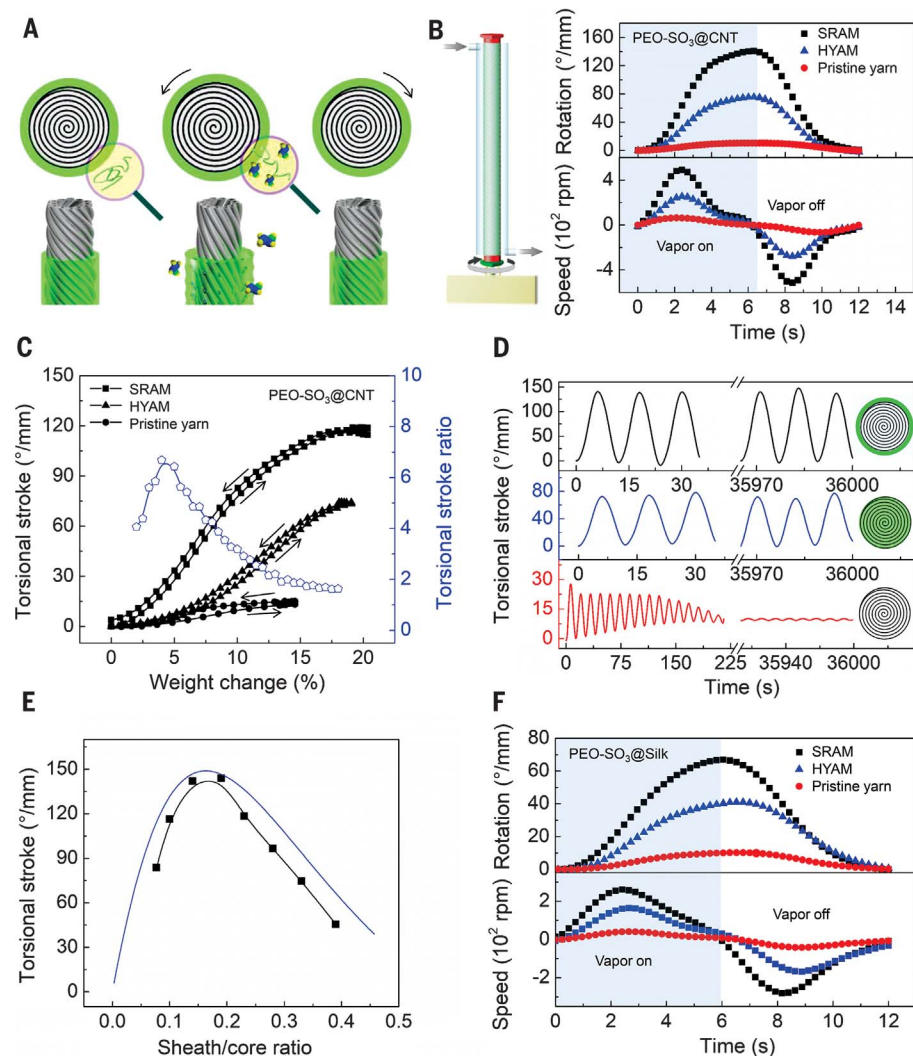


Fig. 2. Torsional actuation of twisted PEO-SO₃ SRAMs and HYAMs driven by ethanol vapor.

(A) Illustrations (left to right) of a PEO-SO₃ SRAM before vapor exposure and during vapor sorption and then desorption, which cause yarn untwist and uptwist, respectively. (B) Illustration of vapor delivery to a muscle and plots of the time dependence of torsional stroke and rotation speed for one sorption-desorption cycle for a PEO-SO₃@CNT SRAM and HYAM and for a pristine CNT yarn. A 41- μ m-diameter pristine yarn, with 72 turns/cm of twist, was used for fabricating the 45- μ m-diameter SRAM and 50- μ m-diameter HYAM, which contained a 0.53 weight ratio of PEO-SO₃ to CNT. (C) Equilibrium torsional stroke versus weight changes (black symbols) during ethanol absorption and desorption for the muscles of (B), and the SRAM-to-HYAM stroke ratio during ethanol absorption (blue pentagons). (D) Torsional stroke versus time for the muscles of (B). (E) The observed (black squares) and predicted (blue line) dependence of torsional stroke on SCR for PEO-SO₃@CNT SRAMs (26). (F) Torsional stroke and rotation speed versus time for a sorption-desorption cycle of a PEO-SO₃@silk SRAM and HYAM and a silk yarn. A 56- μ m-diameter silk yarn (with 5.7 turns/cm of twist) was used for fabricating the 90- μ m-diameter SRAM and HYAM, which weighed 0.48 mg/cm and contained a 0.27 weight ratio of PEO-SO₃ to silk.

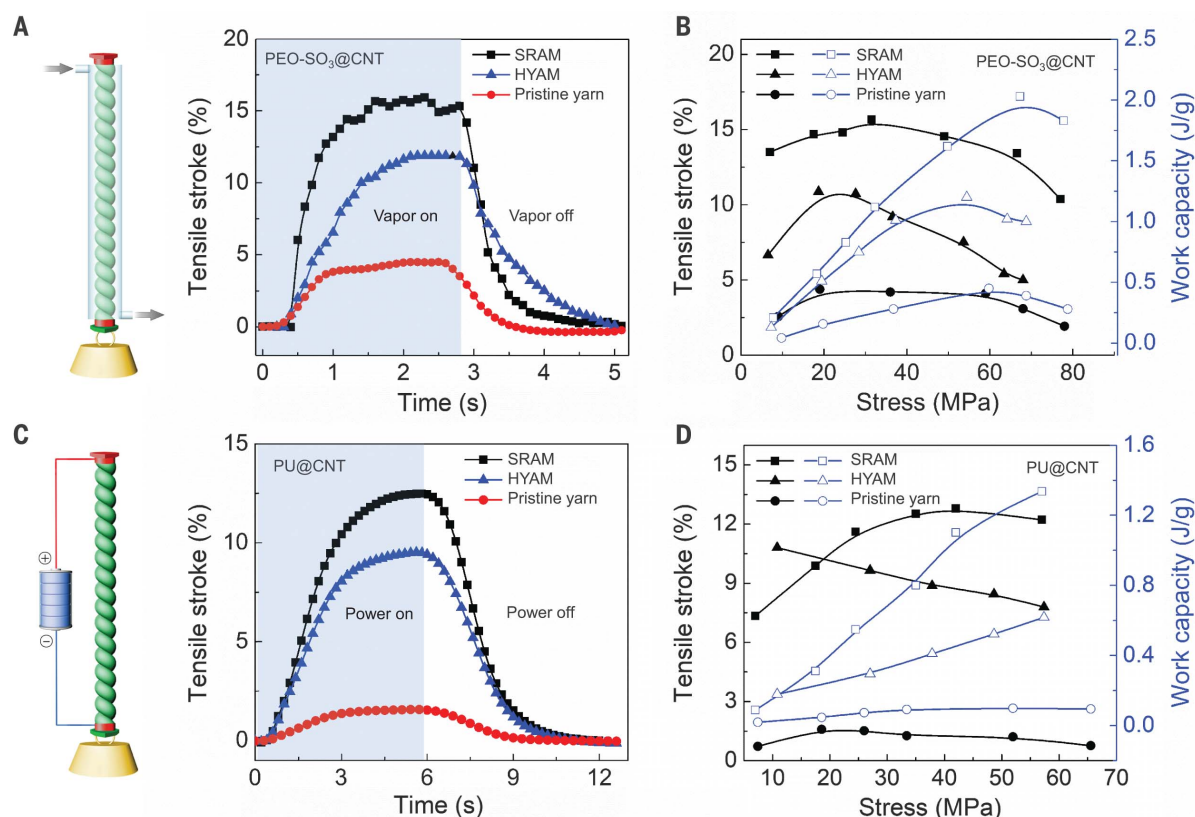


Fig. 3. Isobaric tensile actuation of self-coiled, sorption-powered, and electrothermally powered SRAMs, HYAMs, and pristine CNT yarns.

(A) Tensile stroke versus time for a PEO-SO₃@CNT SRAM and HYAM and a pristine yarn when actuated by ethanol absorption by using the illustrated configuration and 33 MPa stress. Sorption was from a near-equilibrium ethanol concentration in dry air and desorption was by means of dynamic pumping. Before coiling, the diameters of the PEO-SO₃@CNT SRAM and HYAM and the pristine yarn were 43, 47, and 38 μ m, respectively. (B) Tensile stroke and contractile work capacity

versus applied stress for the sorption-actuated muscles of (A). (C) The time dependence of tensile stroke for a PU@CNT SRAM and HYAM and a pristine CNT yarn when electrothermally actuated by using the illustrated configuration, 42 MPa stress, and 0.25 W/cm power, which provided temperatures of 85°, 93°, and 97°C, respectively. (Left) The device structure. Before coiling, the diameters of the PU@CNT SRAM and HYAM and the pristine yarn were 65, 71, and 51 μ m, respectively. (D) Tensile stroke and contractile work capacity versus applied stress for the electrothermally actuated yarns in (C).

Because the electrical energy required for actuation increases with increasing amount of electrochemically accessible CNTs, the contractile work per weight of CNT is an important performance metric. For slow square-wave switching at 10 mHz between 0 and -3 V (Fig. 4C), the load-maximized contractile work capacity is slightly higher for the CNT@nylon6 SRAM (2.35 J/g) than for the CNT HYAM containing the same CNT weight per yarn length (2.01 J/g). However, for more practically applicable actuation rates (fig. S17), the ratios of SRAM to HYAM work capacities for similar tensile loads are much more impressive. For an applied square-wave frequency of ~0.3 Hz, this ratio is ~3.4 for all applied loads. At the highest measured frequency (5 Hz) and the highest applied load, this ratio is 14.6. The electrochemical actuation of a coiled CNT@nylon6 SRAM to provide 14.3% stroke at 0.25 Hz, while lifting a heavy load, is shown in movie S3.

The frequency dependences of work capacity for a coiled CNT@nylon6 SRAM and a coiled CNT HYAM are shown in Fig. 4D for square-wave voltages between 0 and -3 V. For 1 Hz cycle

frequency, the tensile stroke, work per cycle, and average contractile power density for the SRAM were, respectively, 4.7%, 0.99 J/g, and 1.98 W/g, as compared with 0.90%, 0.11 J/g, and 0.22 W/g for the HYAM. The high performance obtained for the SRAM at relatively high frequencies expands the application possibilities for electrochemical artificial muscles.

The contractile energy conversion efficiencies were obtained for optimized voltage scan rates between 0 and -2.7 V. This peak efficiency increased from 2.96% at 80 mV/s scan rate for the CNT yarn muscle to 4.26% at 130 mV/s scan rate for the SRAM (Fig. 4E). Using a higher potential scan rate for both muscles (200 mV/s) (fig. S18), which increased stroke rates, provided a SRAM efficiency (3.8%) that is 2.7 times the HYAM efficiency (26%).

Because the SRAM technology enables replacement of expensive CNT yarns with inexpensive, commercially available polymer yarns whose sheath responds to targeted ambient variables, they are attractive for intelligent structures (29). Relevant for possible use in comfort-adjusting

clothing, SRAMs were knitted into a textile that increased porosity when exposed to moisture, and flat-coil SRAMs were demonstrated (figs. S23 to S25). Analyte-powered sensors that intelligently respond in the body to open and close valves that release drugs in response to antigens (30) or biochemicals such as glucose (31) are other possibilities. A CNT-free SRAM that linearly contracts with increasing glucose concentration was demonstrated (fig. S26), which could squeeze a pouch to release a drug (fig. S20).

The 5.2-, 9.0-, and 9.0-fold advantages at 1 Hz of the SRAM over the corresponding HYAM in electrochemical stroke, contractile work-per-cycle density, and average contractile power density, respectively (Fig. 4D), are important for electrically powered robotic devices in which stroke should be maintained without consuming substantial electrical energy. Electrothermal PEO-SO₃@CNT SRAMs operated in air and in room-temperature water to produce 2.6 W/g (at 9 Hz) and 9.0 W/g (at 12 Hz) of full-cycle contractile power, respectively, compared with the 0.05 W/g typical of human

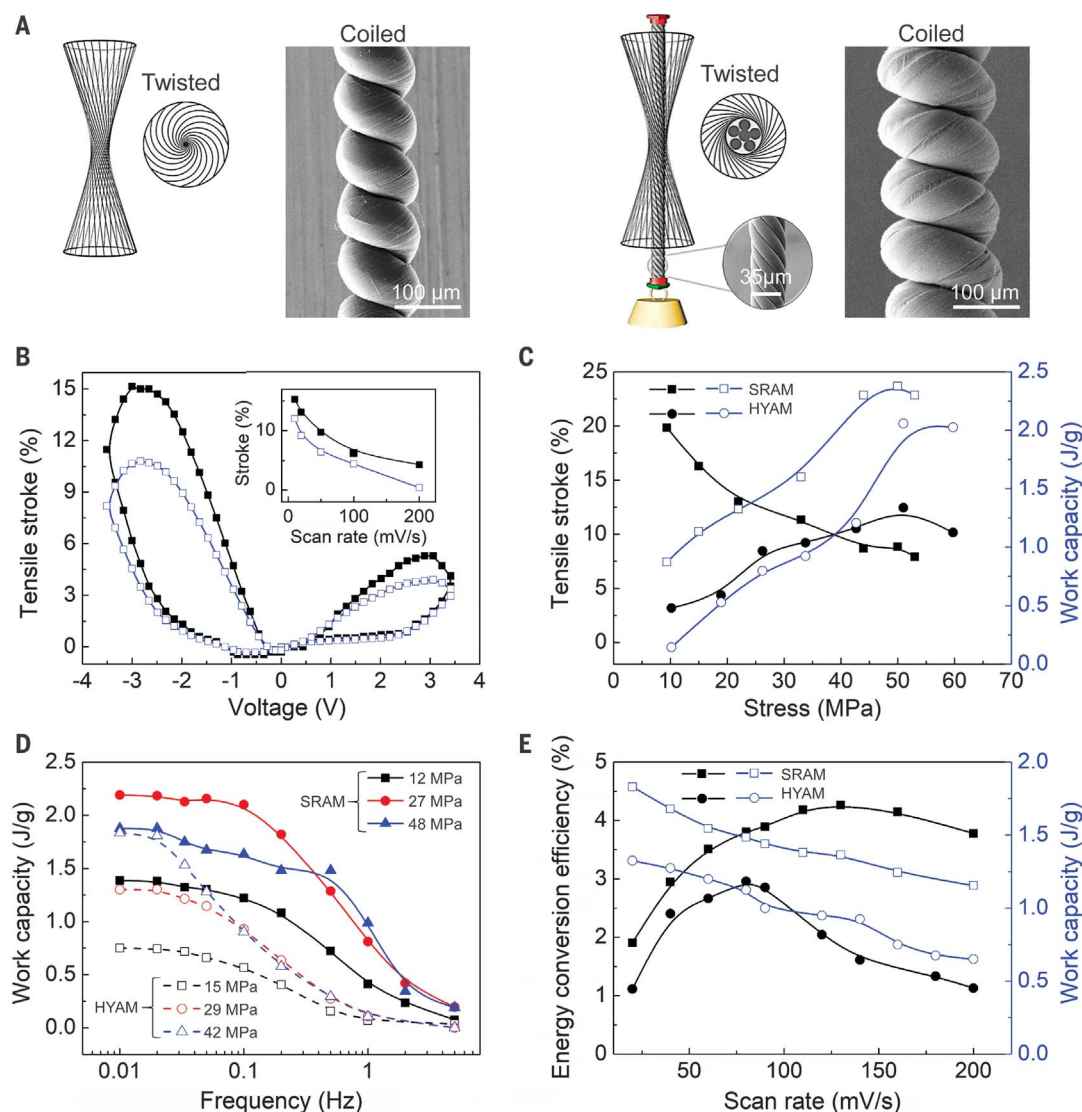


Fig. 4. Fabrication and electrochemical tensile actuation of coiled CNT@nylon6 SRAM and coiled CNT HYAM yarns in 0.2 M TBA- PF_6 /PC electrolyte. (A) Illustration of (left) cone spinning for fabricating CNT yarns and (right) its modification for making SRAM yarns. SEM micrographs of a coiled pristine yarn, a coiled CNT@nylon6 SRAM yarn, and a noncoiled nylon 6 yarn are shown. (B) Tensile stroke of the SRAM and HYAM during a cyclic voltammetry scan at 20 mV/s, under 22 MPa isobaric stress. (Inset) Actuator stroke at this load for this muscle versus interelectrode voltage scan rate. (C) Tensile stroke and contractile work capacity versus load when applying a 10-mHz square-wave voltage between 0 and -3 V. The spring indices of the 95- μm -diameter

CNT@nylon6 SRAM and the 70- μm -diameter CNT HYAM were 0.88 and 0.56, respectively. (D) The frequency dependence of work capacity for a coiled CNT@nylon6 SRAM and a coiled CNT HYAM for square-wave voltages between 0 and -3 V. For 1 Hz cycle frequency, the tensile stroke, work-per-cycle, and average contractile power density for the SRAM at the highest loads were 4.7%, 0.99 J/g, and 1.98 W/g, compared with 0.90%, 0.11 J/g, and 0.22 W/g for the HYAM. (E) The scan rate dependence of work capacity and energy conversion efficiency for the SRAM and HYAM, using an applied stress of ~ 30 MPa for the SRAM and HYAM. For (D) and (E), the spring indices of the 87- μm -diameter CNT@nylon6 SRAM and the 79- μm -diameter CNT HYAM were 0.97 and 0.67, respectively.

muscle (5). SRAM performance and realizable low cost suggests their use for diverse applications, from fast, powerful muscles for humanoid robots and exoskeletons to intelligent comfort-adjusting clothing and drug-delivery systems.

REFERENCES AND NOTES

- M. D. Lima *et al.*, *Science* **338**, 928–932 (2012).
- X. Gu *et al.*, *Nanoscale* **8**, 17881–17886 (2016).
- Y. Sun *et al.*, *Carbon* **132**, 394–400 (2018).
- Y. Song *et al.*, *Nanoscale* **10**, 4077–4084 (2018).
- S. M. Mirvakili, I. W. Hunter, *Adv. Mater.* **30**, 1704407 (2018).
- C. S. Haines *et al.*, *Science* **343**, 868–872 (2014).
- S. H. Kim *et al.*, *Energy Environ. Sci.* **8**, 3336–3344 (2015).
- S. Aziz, S. Naficy, J. Foroughi, H. R. Brown, G. M. Spinks, *Polym. Test.* **46**, 88–97 (2015).
- P. Zhang, G. Li, *Polymer (Guildf.)* **64**, 29–38 (2015).
- M. Hiraoka *et al.*, *Sci. Rep.* **6**, 36358 (2016).
- A. M. Swartz, D. R. Higuera Ruiz, H. P. Feigenbaum, M. W. Shafer, C. C. Browder, *Smart Mater. Struct.* **27**, 114002 (2018).
- H. Cheng *et al.*, *Adv. Mater.* **26**, 2909–2913 (2014).
- J. Fan, G. Li, *RSC Advances* **7**, 1127–1136 (2017).
- S. M. Mirvakili, I. W. Hunter, *ACS Appl. Mater. Interfaces* **9**, 16321–16326 (2017).
- J. Gong, H. Lin, J. W. C. Dunlop, J. Yuan, *Adv. Mater.* **29**, 1605103 (2017).
- C. Lamuta, S. Messelot, S. Tawfik, *Smart Mater. Struct.* **27**, 055018 (2018).
- P. Chen *et al.*, *Nat. Nanotechnol.* **10**, 1077–1083 (2015).
- J. Deng *et al.*, *Nat. Protoc.* **12**, 1349–1358 (2017).
- W. Guo *et al.*, *Adv. Mater.* **24**, 5379–5384 (2012).
- F. Meng *et al.*, *Adv. Mater.* **26**, 2480–2485 (2014).
- I. Agnarsson, A. Dhinojwala, V. Sahni, T. A. Blackledge, *J. Exp. Biol.* **212**, 1990–1994 (2009).
- J. Foroughi *et al.*, *Science* **334**, 494–497 (2011).
- J. A. Lee *et al.*, *Adv. Mater.* **29**, 1700870 (2017).
- S. H. Kim *et al.*, *Sci. Rep.* **6**, 23016 (2016).
- M. D. Lima *et al.*, *Science* **331**, 51–55 (2011).

26. Materials and methods are available as supplementary materials.
27. S. H. Kim *et al.*, *Science* **357**, 773–778 (2017).
28. M. Ue, A. Murakami, S. Nakamura, *J. Electrochem. Soc.* **149**, A1385–A1388 (2002).
29. M. A. McEvoy, N. Correll, *Science* **347**, 1261689 (2015).
30. T. Miyata, N. Asami, T. Uragami, *Nature* **399**, 766–769 (1999).
31. J. Lee *et al.*, *Small* **12**, 2085–2091 (2016).

ACKNOWLEDGMENTS

We thank Lintec of America, Nano-Science and Technology Center for providing CNT forests. **Funding:** Support in the United States was from Air Force Office of Scientific Research grants FA9550-18-1-0510 and FA9550-17-1-0328; Office of Naval Research contract N68335-18-C-0368; National Science Foundation grants CMMI-1661246, CMMI-

1636306, and CMMI-1726435; Robert A. Welch Foundation grant AT-0029; and the Louis Beecherl Jr. Endowed Chair. Australian support was from the Australian Research Council for a Centre of Excellence (CE140100012) and a DECRA Fellowship (DE12010517). Korean support was from the National Research Foundation of Korea for the Creative Research Initiative Center for Self-powered Actuation. Chinese support was from the Science and Technology Commission of Shanghai Municipality (16JC1400700). **Authors contributions:** J.M., M.J.d.A., S.F., N.L., and R.H.B. conceived and initiated the project. All authors contributed to experimental design, planning, and execution; data analysis; and manuscript writing. D.Q., G.S., H.L., X.W., E.G., and R.H.B. built the model. **Competing interests:** J.M., M.J.d.A., S.F., N.L., and R.H.B. are listed as the inventors on a provisional U.S. patent application (62/846,479) that describes sheath-run artificial muscles. **Data and materials availability:** All data

needed to evaluate the conclusions in the paper are present in the paper or the supplementary materials.

SUPPLEMENTARY MATERIALS

science.sciencemag.org/content/365/6449/150/suppl/DC1

Materials and Methods

Supplementary Text

Figs. S1 to S26

Tables S1 and S2

References (32–37)

Movies S1 to S3

11 December 2018; accepted 11 June 2019

10.1126/science.aaw2403

Sheath-run artificial muscles

Jiuke Mu, Mônica Jung de Andrade, Shaoli Fang, Xuemin Wang, Enlai Gao, Na Li, Shi Hyeong Kim, Hongzhi Wang, Chengyi Hou, Qinghong Zhang, Meifang Zhu, Dong Qian, Hongbing Lu, Dharshika Kongahage, Sepehr Talebian, Javad Foroughi, Geoffrey Spinks, Hyun Kim, Taylor H. Ware, Hyeon Jun Sim, Dong Yeop Lee, Yongwoo Jang, Seon Jeong Kim and Ray H. Baughman

Science **365** (6449), 150-155.
DOI: 10.1126/science.aaw2403

Getting the most out of muscles

Materials that convert electrical, chemical, or thermal energy into a shape change can be used to form artificial muscles. Such materials include bimetallic strips or host-guest materials or coiled fibers or yarns (see the Perspective by Tawfik and Tang). Kanik *et al.* developed a polymer bimorph structure from an elastomer and a semicrystalline polymer where the difference in thermal expansion enabled thermally actuated artificial muscles. Iterative cold stretching of clad fibers could be used to tailor the dimensions and mechanical response, making it simple to produce hundreds of meters of coiled fibers. Mu *et al.* describe carbon nanotube yarns in which the volume-changing material is placed as a sheath outside the twisted or coiled fiber. This configuration can double the work capacity of tensile muscles. Yuan *et al.* produced polymer fiber torsional actuators with the ability to store energy that could be recovered on heating. Twisting mechanical deformation was applied to the fibers above the glass transition temperature and then stored via rapid quenching.

Science, this issue p. 145, p. 150, p. 155; see also p. 125

ARTICLE TOOLS

<http://science.sciencemag.org/content/365/6449/150>

SUPPLEMENTARY MATERIALS

<http://science.sciencemag.org/content/suppl/2019/07/10/365.6449.150.DC1>

RELATED CONTENT

<http://science.sciencemag.org/content/sci/365/6449/125.full>
<http://science.sciencemag.org/content/sci/365/6449/145.full>
<http://science.sciencemag.org/content/sci/365/6449/155.full>

REFERENCES

This article cites 37 articles, 9 of which you can access for free
<http://science.sciencemag.org/content/365/6449/150#BIBL>

PERMISSIONS

<http://www.sciencemag.org/help/reprints-and-permissions>

Use of this article is subject to the [Terms of Service](#)



Supplementary Material for **Sheath-run artificial muscles**

Jiuke Mu, Mônica Jung de Andrade, Shaoli Fang, Xuemin Wang, Enlai Gao, Na Li, Shi Hyeong Kim, Hongzhi Wang, Chengyi Hou, Qinghong Zhang, Meifang Zhu, Dong Qian, Hongbing Lu, Dharshika Kongahage, Sepehr Talebian, Javad Foroughi, Geoffrey Spinks, Hyun Kim, Taylor H. Ware, Hyeon Jun Sim, Dong Yeop Lee, Yongwoo Jang, Seon Jeong Kim, Ray H. Baughman*

*Corresponding author. Email: ray.baughman@utdallas.edu

Published 12 July 2019, *Science* **365**, 150 (2019)
DOI: 10.1126/science.aaw2403

This PDF file includes:

Materials and Methods
Supplementary Text
Figs. S1 to S26
Tables S1 and S2
References

Other Supplementary Material for this manuscript includes the following:
(available at science.sciencemag.org/content/365/6449/150/suppl/DC1)

Movies S1 to S3

1. Materials and Fabrication

1.1 Core materials and core yarn fabrication

The MWNT forests used to produce MWNT yarns were ~ 350 μm high, and comprised MWNTs having approximately six walls and an outer diameter of ~ 9 nm. To evaluate the effect of yarn structure on muscle properties, we varied the spinning method to obtain yarns having Archimedean, Fermat, and dual Archimedean structures (*I*), which are illustrated in Fig. S1. By designing the spinning method to insert twist at the center, one edge, and both edges of the spinning triangle, yarns having Fermat, Archimedean, and dual Archimedean structures were obtained. Fermat yarns were directly twist-spun from MWNT forests. By twisting a rigidly end-supported rectangular stack of forest-drawn MWNT sheets, we obtained Archimedean yarns if the applied stress was asymmetric and dual Archimedean yarns if the applied stress was symmetric.

In an exemplary experiment, a 12-cm-long, 2-cm-wide stack of seven sheet layers was twisted to make a MWNT yarn. Inserting 74 turns/cm of twist (normalized to the initial sheet length), while applying 8 MPa stress (normalized to the cross-sectional area of the twisted yarn), produced a 41- μm -diameter yarn with a 42° bias angle. These CNT yarns have either an Archimedean, dual Archimedean, or Fermat structure, depending upon the asymmetry or symmetry of stresses applied during twist insertion

Oriented sheets of electrospun PAN nanofibers with an average diameter of ~ 245 nm were produced by electrospinning using a previously described method (32). In this method, PAN with a weight-average molecular weight of $M_w = 150,000$ g/mol (Aldrich Company) was dissolved in N,N-dimethylformamide by stirring at room temperature overnight to yield an 8 wt% solution. The solution feed rate to the electrospinning needle was $35 \mu\text{L min}^{-1}$, the distance between the needle tip and the two metal wire collectors was about 13 cm, the applied electrostatic field was 0.9 kV/cm, and the metal wire collectors were 12 cm long and separated by 8 cm. Hence, the produced PAN sheet, comprising aligned PAN nanofibers, was 8 cm by 12 cm. Archimedean PAN yarns (Fig. S2 left) were obtained by twisting such PAN sheets. Unless otherwise stated, the PAN and MWNT core yarns had an Archimedean structure.

To provide a well-defined interface between sheath and core, commercially available twisted yarns were inserted with additional twist before the coating process to make SRAMs. On the other hand, since guest penetration into the yarn was needed to make HYAMs, additional twist was inserted into the yarns after guest infiltration. The choice of solvent for guest deposition was adjusted, when needed, to either facilitate complete guest penetration into the cores of HYAMs and to avoid such guest penetration into the cores of SRAMs. In the scanning electron microscope (SEM) images presented here, as well as other images that are not presented, we found that the core of the SRAMs were guest-free and that there were no guest-free regions in the HYAMs.

Table S1 provides the source of commercially obtained silk and bamboo yarns, as well as the initial yarn diameter, the number of fibers in the yarn cross-section and their diameters for the electrospun PAN, silk, bamboo, and nylon 6 yarns.

1.2 Fabrication of SRAMs and HYAMs

The nomenclature used to designate a sheath X on a yarn core Y of a SRAM or a X guest inside a yarn of a HYAM is X@Y. The following polymers were used as sheaths for the non-electrochemical SRAMs and as guests for non-electrochemical HYAMs: polyvinyl alcohol (PVA), nylon 6, two elastomeric polyester-based polyurethanes (PUs) from BASF Corporation (Elastollan[®]1195A10 and TPU-70D, for thermal actuation and sorption-driven actuation,

respectively), and a mixture of polyethylene oxide (PEO) and a co-polymer of tetrafluoroethylene and $F_2C=CF-O-CF_2CF_2-SO_2F$, which we call PEO-SO₃. PVA (7 vol.% concentration in water) and nylon 6 (6 vol.% concentration in formic acid) were purchased from Aldrich Company. The PEO-SO₃ was prepared in aqueous ethanol by mixing PEO (Aldrich Company) and the co-polymer of tetrafluoroethylene and $F_2C=CF-O-CF_2CF_2-SO_2F$ (Aquivion® PFSA from the Solvay Group) at a weight ratio of 3:7.

Uniform sheaths were deposited at room temperature in air on core yarns by manually drawing droplets of the viscous sheath polymer solution along the length of the vertically suspended core yarn, while the yarn was torsionally tethered to prevent yarn untwist. Depending upon the desired thickness of the sheath, this droplet-coating method was repeated multiple times. After complete drying in air to remove solvent, the sheath/core ratio (SCR, which is the ratio of the sheath thickness to the diameter of the interior yarn) was measured using a SEM.

The above droplet deposition process was modified in order to infiltrate a guest polymer into a core yarn to make a HYAM, rather than to coat the core yarn to make a SRAM. This modification was of two types. First, the solvent used for polymer infiltration was selected to enable wetting of the core yarn. For instance, while PEO-SO₃ SRAM fabrication used an ethanol-to-water weight ratio of 5:5 as the solvent, an ethanol-to-water-to-formic acid ratio of 8:1.5:0.5 was deployed for making a PEO-SO₃ HYAM. Additionally, the infiltration process for fabricating the HYAMs occurred while the yarn was in a less twisted state (i.e., having lower twist density) than used for depositing the sheath of a SRAM. After this deposition, while the guest was in a gel-like state, additional twist was inserted to ensure that the degree of twist in the HYAM was identical to that in the SRAM.

According to the type of core yarn and the desired actuator properties, the coiled muscles used for tensile actuation were made either by self-coiling a twisted SRAM or a twisted HYAM (meaning inserting twist until complete yarn coiling occurred) or by wrapping a twisted or self-coiled SRAM or twisted or self-coiled HYAM around a mandrel. After these coiling processes, the coiled SRAMs or coiled HYAMs were thermally annealed. The annealing conditions for the guests were 4 hours at 115°C for PEO-SO₃, 2 hours at 60°C for PU, and 2 hours at 180°C for nylon 6. The fabrication of the electrochemical muscles is described in the main text. The stresses applied during twist insertion and self-coiling were identical, and are normalized with respect to the cross-sectional area of the twisted yarn muscle before annealing. The tensile stress during actuation was normalized in the same way.

The SEM micrograph of Fig. S2A (right) for a PEO-SO₃@PAN SRAM and Figs. 1C and S3A for a PEO-SO₃@CNT SRAM show that the guest in the sheath does not infiltrate into the muscle core. Complete infiltration of the guest into the core yarn is shown in Fig. S3B for a PEO-SO₃@CNT HYAM. The SEM images of Fig. S3 were obtained by sectioning the PEO-SO₃@CNT SRAM and HYAM using Ga ions (5 nA beam current) in a Focused Ion Beam (FIB, Nova 2000) operated at 30 kV, followed by ion-polishing (consecutively decreasing ion-currents from 3.0 to 0.3 nA). The inset of Fig. S3A shows that the core CNT yarn can be pulled from the PEO-SO₃@CNT SRAM, thereby leaving only the PEO-SO₃ sheath. To accomplish this extraction, the PEO-SO₃@CNT SRAM was embedded in epoxy, and then the embedded SRAM was fractured while in liquid N₂.

The spring index of a coiled muscle is an important parameter for determining muscle stroke. The spring index is defined as the ratio of the difference in outer coil diameter and the fiber diameter to the fiber diameter, where a fiber's diameter is its width in its largest lateral dimension. Since highly coiled yarns become elliptical as a result of coiling, the spring index can

be smaller than unity.

1.3 Characterization of key guest materials

The time dependence of Young's modulus during ethanol sorption and desorption by a 75- μm -thick, 5×30 mm sheet of PEO-SO₃ was measured using an Instron 5848 Microtester (Fig. S4A). To determine the temperature range useable for reversible thermal actuation of PEO-SO₃@CNT, we evaluated the thermal stability range of PEO-SO₃ by using thermogravimetric analyses (TA Instruments Q600 Thermogravimetric Analyzer). These results (Fig. S4B) show an initial weight loss of 8% up to $\sim 280^\circ\text{C}$ on heating ($5^\circ\text{C}/\text{min}$ in air), which results from desorption of water. Above this temperature, the polymer thermally degrades. Since the maximum temperature used for thermal actuation is 180°C , thermal degradation does not significantly occur during actuation.

We characterized the effects of solvent absorption/desorption on guest volume. By recording the dimensions of a polymer sheet as a function of time during exposure to 0.234 mg/L of ethanol vapor in dry atmospheric pressure air (using time-lapse photography), the equilibrium percent volume change of PEO-SO₃, PVA and nylon 6 guests were measured (Fig. S5A). This 0.234 mg/L of ethanol approximately corresponds to a saturated atmosphere of ethanol in dry, room-temperature air.

2. Method and Apparatus for Characterizing Actuation

Torsional and tensile electrothermal and absorption-driven actuation were characterized by using a commercial laser proximity sensor system (Keyence Corporation of America), which captured either the rotation of a paddle or the displacement of a weight attached at the end of the muscle. The electrothermal measurements were for muscles that used a carbon nanotube yarn as the heating element. Measurements using the proximity sensor were complemented by results obtained by frame-by-frame analysis of movie pictures taken using CASIO 12.5HS and Canon EOS 500D cameras. Thermal tensile actuation was characterized using a TA Instruments TMA Q400 thermomechanical analyzer, at heating and cooling rates of $5^\circ\text{C}/\text{minute}$. Vapor-driven actuation used the equilibrium vapor pressure of a liquid in dry, room-temperature air. For comparative studies, the same lightweight paddle at yarn end (weighing 60 mg, and having a moment of inertia of $0.28 \text{ kg}\cdot\text{mm}^2$) was used to characterize torsional rotation angle and speed.

Electrochemical measurements of tensile actuation used an artificial muscle working electrode and a high capacitance counter electrode (a CNT-covered Pt mesh), and measured voltages are between these two electrodes. A contactless inductive proximity sensor (Omega LD701 5/10) and Laser Displacement Sensor (Keyence CD33) with data acquisition (Omega module OM-USB-1408Fs) were used to record the displacement of a weight attached at the end of a muscle.

Unless otherwise indicated, all stresses are nominal values determined by normalizing applied force to the cross-sectional area of the non-loaded, non-actuated twisted muscle and the torsional stroke was normalized to the loaded length of the muscle. Unless otherwise described for plots of actuation versus time, actuation was reversed after essentially the entire muscle stroke was realized (as indicated by previous measurements of muscle stroke versus time, where actuation was observed until muscle stroke because essentially constant).

3. Characterization of Torsional Actuation

3.1 Effect of scroll structure and inserted twist on torsional actuation of SRAMs

The results of Fig. S1 show that the scroll type of a CNT SRAM core importantly affects

torsional actuation. More specifically, an Archimedean core structure provides higher torsional stroke and a higher peak rotation speed than either a Fermat or a dual-Archimedean core SRAM, and the stroke and peak rotation speed of the dual-Archimedean SRAM are lowest. This low performance of the dual-Archimedean SRAM is understandable, since this SRAM has two centers of torsional rotation, rather than the one center found for the other core structures.

Inserting twist into a yarn comprising fibers that are oriented along the yarn direction causes the fibers to become oriented at an angle with respect to the yarn direction, which is called the bias angle. This bias angle is maximum on the yarn surface and decreases to zero as the radial distance from yarn center decreases to zero. Unless otherwise indicated, the yarns bias angle means the bias angle on the yarn's surface. Since dual-Archimedean yarns have two centers of twist insertion, the bias angle is more difficult to describe for these yarns. In the below analysis, we will determine the effect of a yarn's bias angle on actuation.

Figure S6 shows that the equilibrium torsional stroke of an ethanol-absorption-driven PEO-SO₃@CNT SRAM having a sheath-to-core weight ratio of about 0.53. This stroke rapidly increases with the increasing CNT yarn bias angle until the stroke reaches a plateau at ~38° and then decreases for bias angles above ~42°, where yarn coiling is initiated. The ratio of torsional stroke to inserted twist reaches a peak at ~27° and decreases at higher angles. Figure S2B compares the torsional actuation of a PEO-SO₃@PAN SRAM and HYAM and a pristine yarn when undergoing one reversible cycle of ethanol vapor sorption and desorption.

The results of Fig. S6 can be used to predict the equilibrium torsional stroke of an ethanol-vapor-driven PEO-SO₃@CNT SRAM having any diameter and bias angle. The torsional stroke and yarn diameter as a function of yarn bias angle are provided in this figure. Since the product of torsional stroke and yarn diameter is invariant when the yarn's bias angle is constant (6), the stroke for a new core yarn is obtained by dividing this product by the diameter of the new yarn. For comparison with results for a PEO-SO₃@PAN SRAM (Fig. S2B) and a PEO-SO₃@silk SRAM (Fig. 2F), respectively, a PEO-SO₃@CNT SRAM with a 76 µm core diameter and a 30° bias angle has a predicted stroke of 93°/mm and a PEO-SO₃@CNT SRAM with a 56 µm core diameter and an 18° bias angle has a predicted stroke of 66°/mm. These results are close to the observed 123°/mm for the PEO-SO₃@PAN SRAM and the 70°/mm for the PEO-SO₃@silk SRAM.

3.2 Effect of guest on the torsional actuation of ethanol-vapor-driven SRAMs

Figure S5B shows that the torsional stroke of the PEO-SO₃@CNT SRAM (143°/mm) is giant compared with that for PVA@CNT SRAM (22°/mm) and nylon6@CNT SRAM (11°/mm). This relatively giant stroke of the PEO-SO₃@CNT SRAM can not be explained by only considering the much larger percent volume change of the PEO-SO₃ (16.7%) than for the PVA (1.3%) and nylon 6 (0.5%), as shown in Fig. S5A. This is indicated by the fact that the ratio of the diameter-scaled torsional stroke (the product of torsional stroke and muscle diameter) to the percent volume change of the sheath is not constant, and varies from 0.6 for a PEO-SO₃@CNT SRAM to 1.6 for a PVA@CNT SRAM to 1.9 for a nylon6@CNT SRAM. The sheath/core ratio of these SRAMs are similar, varying from 0.12 and 0.14 for nylon 6 and PEO-SO₃, respectively, to 0.17 for PVA.

3.3 Effect of sheath/core ratio on the fabricability and ethanol-vapor-driven torsional actuation of a twisted PEO-SO₃@CNT SRAM

Figure S7A shows the combinations of sheath/core ratio and yarn bias angle that result in sheath cracking (red region) during release of torsional tethering during the final step of twisted SRAM fabrication, and combinations that result in crack-free sheaths (white region). The data

points denote the maximum bias angle that can be inserted for a given sheath/core ratio without causing cracks in the sheath of the SRAM. Figure S7B shows the dependence of torsional stroke and maximum rotation speed on sheath/core ratio for a non-coiled 39- μm -diameter PEO-SO₃@CNT SRAM containing 74 turns/cm of twist. These results indicate that a sheath/core ratio of ~ 0.14 enables a bias angle of 42° (corresponding to 74 turns/cm of inserted twist) without crack formation. The decrease in both maximum rotation speed and torsional stroke for sheath/core ratios above ~ 0.2 results from mechanical hinderance of torsional rotation by a sheath thickness that is too high. The blue line is the theoretically predicted dependence of torsional stroke on sheath/core ratio (Section 5), which agrees with the experimental results (Fig. 2E). Figure S7 C-F shows, for a large range of sheath-core ratios, that the PEO-SO₃@CNT SRAMs have a sheath-core structure in which the sheath does not infiltrate into the core yarn.

3.4 Effect of different vapors on the torsional actuation of a PEO-SO₃@CNT SRAM

Of the investigated solvents, ethanol provided the largest torsional stroke for a PEO-SO₃@CNT SRAM. However, the results in Fig. S8 show that usefully large torsional strokes can also be obtained for this SRAM when using various other vapors in saturated room temperature air. These results were obtained using the same SRAM as deployed for Fig. 2B and C.

3.5 Comparison of sorption driven torsional actuation of a nylon6@CNT SRAM, a nylon6@CNT HYAM, and a neat CNT yarn

The results of the present study demonstrate that similar performance advantages of SRAM structure over the hybrid yarn structure can be obtained when ethanol-driven PEO-SO₃@CNT muscles are replaced by water-vapor-driven nylon6@CNT muscles. Figure S9 shows the time-dependence of torsional rotation angle and torsional rotation speed for water-vapor-driven torsional actuation of a 43.7- μm -diameter nylon6@CNT SRAM, a 47- μm -diameter nylon6@CNT HYAM, and a 39- μm -diameter pristine CNT yarn. The performance advantage of using a SRAM, compared with using a HYAM, is nearly the same as for the PEO-SO₃@CNT muscles of Fig. 2B. Specifically, the SRAM to HYAM torsional stroke ratio and maximum torsional speed ratio for the nylon6@CNT muscles are 1.63 and 1.86, respectively, compared to 1.86 and 1.75, respectively, for the PEO-SO₃@CNT muscles.

4. Characterization of tensile actuation

4.1 The effect of torsional tethering on the ethanol-vapor-driven tensile actuation of a twisted PEO-SO₃@CNT SRAM

Figure S10 shows the effect of torsional tethering on the time-dependence of tensile stroke during actuation of an ethanol-vapor-driven twisted PEO-SO₃@CNT SRAM. Actuation was produced by exposure of the muscles to 0.234 mg/L of ethanol in dry air, and actuation was reversed by desorbing the ethanol using dynamic pumping. These results indicate that the tensile stroke of a torsionally-tethered SRAM (3.07%) is much larger than for a SRAM that is free to rotate (1.25%). The larger tensile stroke for the torsionally tethered SRAM than for the non-torsionally-tethered SRAM is understandable, since torsional untwist during actuation causes the yarn to elongate. This tensile stroke for the torsionally-tethered twisted SRAM is much smaller than for an identical SRAM that is coiled and torsionally tethered (Fig. 3A), which has a maximum tensile stroke of 15.7%.

4.2 Comparison of ethanol-vapor-driven tensile actuation of a coiled PEO-SO₃@CNT SRAM, a coiled PEO-SO₃@CNT HYAM, and a coiled neat CNT yarn

Figure S11 shows the time-dependence of tensile stroke for an ethanol-vapor-driven coiled PEO-SO₃@CNT SRAM, a coiled PEO-SO₃@CNT HYAM, and a coiled pristine yarn that were

torsionally tethered. Actuation cycles were obtained by exposing the muscles to dry air containing 0.17 mg/L of ethanol and then desorbing the ethanol using dynamic pumping. Before coiling, these actuating structures had similar diameters (43, 47, and 38 μm , respectively), and the applied stress during coiling and actuation were 8 MPa and 33 MPa, respectively, for all structures. All muscles contained the same weight of CNTs per untwisted length, and both PEO-SO₃@CNT muscles have similar linear densities (0.33 mg/cm before coiling). The spring indices of the SRAM, the HYAM, and the pristine yarn were 0.51, 0.56, and 0.32, respectively. The observed tensile stroke for the coiled pristine yarn is small (2.1%), compared to that of the coiled PEO-SO₃@CNT SRAM (15.1%) and the coiled PEO-SO₃@CNT HYAM (9.6%). The ratio of tensile stroke for the coiled PEO-SO₃@CNT SRAM to that of the coiled PEO-SO₃@CNT HYAM is high (1.57), despite the slightly lower spring index of the SRAM (0.51) compared to that of the HYAM (0.56). The higher maximum contraction rate of the SRAM (3.2 %/s) compared to that of the HYAM (1.5 %/s) provides an additional performance benefit of the SRAM compared to the HYAM. These results are for actuation using dry air containing 0.17 mg/L of ethanol. Hence, as shown in the next paragraph, both the maximum stroke and maximum stroke rate can be increased by increasing the ethanol concentration to its equilibrium value in dry, room-temperature air (0.234 mg/L).

For the same coiled PEO-SO₃@CNT SRAM as used above, Fig. S12A shows the dependence of equilibrium isometric tensile stress generation on the concentration of ethanol in dry air. These results indicate that the generated tensile stress is reversibly related to the concentration of ethanol vapor, reaching a maximum of 68 MPa at an ethanol concentration of 0.234 mg/L. When this SRAM was operated isobarically at 33 MPa using a saturated atmosphere of ethanol in dry air, a tensile contraction of 14.3% was obtained in 1.2 s, to provide an average contraction rate of 10.6 %/s (Fig. 3A).

Figure S12B shows the dependence of load-optimized work capacity of a coiled PEO-SO₃@CNT SRAM and HYAM as a function of guest-to-host weight ratio. The weight ratio at which the guest PEO-SO₃ begins to extrude from the HYAM during coiling is around 1.2. Increases of the weight ratio to above 1.2 results in a muscle whose performance combines both SRAM and HYAM types of actuation. For a guest-to-host mass ratio (M_G/M_H) of above 2.1 (Fig. S12B), this combination of SRAM and HYAM actuation provides a slightly higher work capacity than does a SRAM whose sheath is so thick that it constrains twist release. However, the peak in work capacity for the SRAM is still 1.6 times that for the muscle that combines sheath-run and HYAM types of actuation.

Figure S12C shows the effect of using an overly thick sheath on the actuation of a SRAM when the applied mechanical load is small. Actuation was produced by dropwise addition of ethanol to a PEO-SO₃@PU SRAM that had a sheath/core ratio of 2.27. During addition of the ethanol, muscle contraction occurs until inter-coil contact results. With further addition of ethanol, additional sheath expansion causes the muscle to expand. Upon evaporation of the ethanol, the muscle initially contracts and then expands to reverse the actuation process.

While self-coiled structures provide the highest work capacity, because of their low spring indices and correspondingly high tensile moduli, the contraction during tensile actuation can be amplified by using mandrel-coiled muscles having very high spring indices. This amplification is evident in the plots of Fig. S13 of contractile strain versus time for water-vapor-driven actuation of cylindrical and cone-shaped PEO-SO₃@CNT SRAMs that have coiled and supercoiled structures.

4.3 Comparison of thermal and electrothermal tensile actuation of SRAMs and HYAMs based on PEO-SO₃@CNT and nylon6@CNT yarns

Figure S14 compares the stress dependence of tensile stroke and contractile work capacity for a PEO-SO₃@CNT SRAM and a PEO-SO₃@CNT HYAM for a temperature increase from 25°C to 200°C. The contractile work capacity for both the SRAM and the HYAM increases monotonically with applied load, as does the ratio of SRAM to HYAM contractile work capacity (which is 1.5 for a tensile stress of 45 MPa).

The results of Fig. S15A, B are for the electrothermal actuation of a PEO-SO₃@CNT SRAM, a PEO-SO₃@CNT HYAM, and a pristine CNT yarn by providing a power input per yarn length of 0.18 W/cm. A 0.08 Hz square-wave potential was applied, which provided peak temperatures of 167, 175, 190°C, respectively, for the three yarn types, which are far below the temperature at which thermal degradation occurs for the PEO-SO₃ (Fig. S4B). The tensile contraction and load-optimized contractile work capacity of the SRAM (8.04% and 0.64 J/g) was significantly larger than for the HYAM (5.53% and 0.37 J/g), and the tensile contraction and load-optimized contractile work capacity of the pristine CNT yarn (1.95% and 0.10 J/g) were small. The ratios of tensile strokes and maximum contractile work capacities of the SRAM to that of the HYAM were 1.45 and 1.73, respectively, up to loads that cause muscle damage).

The frequency dependence of average-stroke-release rate for an electrothermally powered muscle (Fig. S15 C and E) show that the rate of cooling is much faster for the SRAM than for the HYAM when the muscles are driven in either air or in a room temperature bath water using a constant voltage pulse. Since the cooling rate has the greatest impact on full cycle performance (especially when the muscle is running at a high frequency), the work capacities per thermal cycle and the full-cycle contractile power densities for the SRAM are much higher than for the corresponding HYAM for high frequencies at which either muscle provides a useful work capacity (Fig. S15D and F). Since these results are for a constant applied square-wave voltage pulse (0 to 12 V in air for Fig. S15 C, D and 0 to 23 V in room temperature water for Fig. S15 E, F) decreasing input electrical energy with increasing frequency affected these results by causing the work capacity to decrease earlier than it would if the energy input during a cycle were constant.

The results of Fig. S16 show that, for all temperature changes, the thermal actuation stroke of a nylon6@CNT SRAM is significantly larger than a nylon6@CNT HYAM, and that the thermal stroke of a pristine CNT yarn is too small to be useful. For these comparative results, the same amount of CNT sheet was used to prepare the three yarns and the weight of nylon 6 per muscle length before coiling was the same for the SRAM and for the HYAM, which resulted in a linear density of 0.33 mg/cm for both muscles before coiling. Results at a 5°C/minute scan rate (Fig. S16) show that the stroke of a SRAM can exceed that of a HYAM even when the SRAM has a lower spring index and the actuation rate is low.

4.4 Comparison of electrochemical tensile actuation of a coiled CNT@nylon6 SRAM and a coiled CNT yarn in 0.2 M TBA·PF₆ (tetrabutyl ammonium hexafluorophosphate in propylene carbonate)

Figure S17 shows that the ratio of contractile work capacities of the electrochemical SRAM to the electrochemical HYAM (i.e., the neat yarn) dramatically increases with increasing cycling frequency.

The contractile energy conversion efficiency for converting electrical energy to contractile mechanical energy was maximized for both the SRAM and HYAM by varying voltage scan rates for between 0 and -2.7 V. The electrical energy input during muscle charging

and the electrical energy output during muscle discharge for the SRAM (54.0 and -22.0 J/g) and for the CNT yarn (58.1 and -20.1 J/g) are similar, while the maximum contractile mechanical energy output (Fig. 4E) for the SRAM (1.363 J/g at 130 mV/s scan rate) is higher than for the CNT yarn (1.125 J/g at 80 mV/s scan rate). This maximum efficiency increased from 2.96% for the CNT yarn muscle to 4.26% for the SRAM (Fig. 4E).

While using a higher voltage scan rate than the above rates decreases the contractile efficiency of both SRAM and HYAM, such higher scan rates increase stoke rates. Hence, we next compare contractile energy conversion efficiencies of both SRAM and HYAM for a voltage scan rate of 200 mV/s. As shown in Fig. S18, the electrical energy input during muscle charging and the electrical energy output during muscle discharge for the SRAM (57.3 and -25.8 J/g) and for the CNT yarn (65.8 and -23 J/g) are similar at this voltage scan rate. However, the net electrical energy cost for an actuation cycle of the SRAM (31.5 J/g) is lower than that for the CNT yarn (42.8 J/g), while the contractile mechanical energy output (Fig. 4E) for the SRAM (1.2 J/g) is higher than for the CNT yarn (0.6 J/g). Consequently, the contractile energy efficiency of the SRAM is 3.8% versus 1.4% for the HYAM.

Although a slightly higher contractile efficiency has been previously reported (4.5%) for a two-ply coiled CNT yarn than for the SRAM (4.26%) when operated in the same electrolyte (23), this peak contractile efficiency was for a potential scan rate that is 6.5 times lower than the scan rate (and full cycle actuation time) that maximized the contractile efficiency of the SRAM (130 mV/s).

4.5 Maximum average contractile power

Maximum average contractile power is defined as the maximum ratio of contractile work to actuation time. Results for maximum average contractile power for tensile actuation of various types of SRAMs are shown in Fig. S19. These results are for the tensile load that maximizes contractile work. Table S2 summarizes the measured contractile work capacities and maximum average power densities for vapor-driven, thermally-driven, and electrochemically-driven SRAMs and HYAMs. Reflecting the shorter diffusion distance to fully access the sheath of a SRAM than to fully access the core of a HYAM for ethanol-vapor-driven PEO-SO₃@CNT muscles, the SRAM-to-HYAM ratios for contractile power are a factor of ~1.65 times the corresponding ratio for equilibrium contractile work (Table S2). In contrast, the SRAM-to-HYAM ratios for contractile power are similar to those for equilibrium work for both PEO-SO₃@CNT and PU@CNT muscles that are internally driven by electrothermally heating the CNT yarn.

4.6 A cylindrical braid that changes structure because of the water-driven actuation of a coiled PEO-SO₃@bamboo SRAM

Figure S20 shows the morphing of a cylindrically braid, like in a McKibben muscle (33), by the water-absorption driven contraction of a coiled PEO-SO₃@bamboo SRAM that is inside a McKibben structure made of nylon 6 fibers. A bio-responsive SRAM could be used as the yarns of a braided cylinder (like in Fig. S20), so that muscle contraction squeezes a pouch to release a drug that is within the hollow braid. Alternatively, parallel bio-response SRAMs could be located in a mechanically balanced manner on the exterior of the woven braid, and mechanically connected to it, to provide release of a drug that is within the braid. By combining muscle segments that respond to different bioagents, such as different antigens (either by adding to or cancelling muscle response), drug release could be made intelligent.

5. Prediction of the dependence of absorption-driven torsional actuation on the sheath/core ratio

Corresponding to the method presently used to make twisted SRAMs, this theoretical analysis considers a SRAM core yarn having an initial twist of T_0 (turns per muscle length), which is clamped at both ends and coated with the sheath material until the sheath dries to set the initial state of the SRAM. If the yarn was unclamped before the sheath was applied, then the yarn will decrease twist by ΔT_0 due to elastic removal of most of the inserted twist. The fully-dried SRAM is unclamped at one end allowing rotation that removes a twist of ΔT_{off} from the core yarn, and introduces twist into the SRAM's sheath. In the equilibrium non-actuated state, the torque on the core yarn is balanced by the opposing torque in the elastically twisted sheath, so that:

$$0 = k_{\text{core}}^{\text{off}}(\Delta T_0 + \Delta T_{\text{free,off}} - \Delta T_{\text{off}}) - k_{\text{sheath}}^{\text{off}}\Delta T_{\text{off}}, \quad (5.1)$$

where $k_{\text{core}}^{\text{off}}$ and $k_{\text{sheath}}^{\text{off}}$ are the torsional stiffnesses of the core and sheath, respectively, in the non-actuated state and $\Delta T_{\text{free,off}}$ is the change in core twist due solely to the compression applied by the drying sheath. The corresponding torsional stiffnesses for the actuated state are $k_{\text{core}}^{\text{on}}$ and $k_{\text{sheath}}^{\text{on}}$, respectively. Rearranging Eqn. 5.1 gives:

$$\Delta T_{\text{off}} = (\Delta T_0 + \Delta T_{\text{free,off}})/(1 + k_{\text{sheath}}^{\text{off}}/k_{\text{core}}^{\text{off}}). \quad (5.2)$$

Using the above approach, we can now calculate the twist change (ΔT_{on}) in going from initial yarn twist (T_0) to the twist that results from actuation of the SRAM. Now the torque balance equation is written as:

$$0 = k_{\text{core}}^{\text{on}}(\Delta T_0 + \Delta T_{\text{free,on}} - \Delta T_{\text{on}}) - k_{\text{sheath}}^{\text{on}}\Delta T_{\text{on}} \quad (5.3)$$

where $\Delta T_{\text{free,on}}$ is the change in core twist due solely to the expansion applied by the actuating sheath.

Hence,

$$\Delta T_{\text{on}} = (\Delta T_0 + \Delta T_{\text{free,on}})/(1 + k_{\text{sheath}}^{\text{on}}/k_{\text{core}}^{\text{on}}). \quad (5.4)$$

The torsional stroke of the SRAM is:

$$\Delta T_{\text{SRAM}} = \Delta T_{\text{on}} - \Delta T_{\text{off}}. \quad (5.5)$$

Since the modulus of the yarn in the axial direction is much higher than in radial directions, we can approximate that the length of the twisted SRAM does not change during torsional actuation.

Hence, we approximate that the change in twist of the yarn core occurs without energetically costly changes in SRAM length. Correspondingly, the helix equation (1, 34) gives that the fractional change in twist equals the fractional change of the diameter of the core yarn.

Consequently, we obtain that:

$$\Delta T_{\text{free,on}} = (T_0 + \Delta T_0)(d_{\text{core}}^{\text{Uncoated}}/d_{\text{core}}^{\text{on}} - 1) \text{ and} \quad (5.6)$$

$$\Delta T_{\text{free,off}} = (T_0 + \Delta T_0)(d_{\text{core}}^{\text{Uncoated}}/d_{\text{core}}^{\text{off}} - 1), \quad (5.7)$$

where the yarn core diameters in the uncoated, actuation-off, and actuation-on states are $d_{\text{core}}^{\text{Uncoated}}$, $d_{\text{core}}^{\text{off}}$ and $d_{\text{core}}^{\text{on}}$, respectively.

The core diameter of the SRAM after drying in the non-actuated state ($d_{\text{core}}^{\text{off}}$) is estimated by first considering the compression ratio $\lambda = d_{\text{core}}^{\text{on}}/d_{\text{core}}^{\text{off}}$. This compression ratio, which is a function of the sheath/core ratio (SCR), can be evaluated from elasticity theory by drawing analogy to the case where a core cylinder is inserted into a hollow tube that has an initial inner

radius that is smaller than the initial radius of the core cylinder. Using literature results (35), λ is obtained from:

$$\lambda = 1 - (1 - \varphi)/[\lambda E_s/E_c(((1 + 2SCR/\lambda)^2 + 1)/((1 + 2SCR/\lambda)^2 - 1) + \nu_s)/(1 - \nu_c) + \lambda], \quad (5.8)$$

where φ is the ratio of the sheath thickness in the non-actuated state to the sheath thickness in the actuated state. E_s and E_c are the elastic moduli of the sheath and the core, respectively, in the radial direction, and ν_s and ν_c are the corresponding Poisson's ratios that couple a stretch in the circumferential direction to the deformation in the radial direction.

We next apply these theoretical results to the specific case of predicting the dependence of torsional actuation on sheath/core ratio for ethanol-driven actuation of a PEO-SO₃@CNT SRAM. Since experimental measurements (Fig. S4A) show that the Young's modulus for the sheath of the ethanol-saturated SRAM is very low (50.4 MPa), the stresses on the SRAM core are similar for the actuated state and the initial uncoated state (which are like those for the undried-sheath state). Hence, we approximate that $d_{\text{core}}^{\text{Uncoated}} = d_{\text{core}}^{\text{on}}$.

Solving Eqns. 5.5-5.8, using measured values of the Young's moduli of sheath and core (294 MPa and 354 MPa, respectively, in the non-actuated state), the Poisson's ratios of sheath and core (0.40 and 0.18, respectively), and the relationship for an isotropic material between these parameters and the shear modulus for the sheath, shear moduli of 105 MPa and 150 MPa are calculated for the non-actuated state of the PEO-SO₃ sheath and the CNT core yarn, respectively. Even though the core structure is not three-dimensionally isotropic, this assumption is appropriate since the core elastic properties are transversely isotropic. The relationship between shear modulus (G) and torsional stiffness (k) for a rod of length (L) and cross-sectional polar 2nd moment of area (J), which is $k=GJ/L$, is here exploited. The diameter of the core of the SRAM is 35.0 μm , and the thickness of sheath can be calculated from the SCR and the diameter of the core. For the HYAM, the host and guest co-share the same yarn volume and the yarn diameter is 44.2 μm . The lengths of the SRAM and HYAM are both 48.0 mm.

Calculation of the torsional stiffness for the HYAM proceeds analogously, except that the rule-of-mixtures is used to calculate the effective shear modulus of the HYAM. Consequently, for the non-actuated state, we obtained the torsional stiffness of the sheath of the SRAM (4.90×10^{-10} N·m/rad), the core of the SRAM (3.93×10^{-10} N·m/rad), the yarn host of the HYAM (7.10×10^{-10} N·m/rad), and the guest of the HYAM (3.23×10^{-10} N·m/rad). Similarly, using measured values of the Young's moduli of sheath and core (50.4 MPa and 302.8 MPa, respectively, in the actuated state), the Poisson's ratios of sheath and core (0.4 and 0.18, respectively), and the relationship for an isotropic material between these parameters and the shear modulus, shear moduli of 18 MPa and 128 MPa are calculated for the actuated state of the PEO-SO₃ sheath and the CNT core yarn, respectively. Likewise, for the actuated state, we obtained the torsional stiffness of the sheath of the SRAM (1.21×10^{-10} N·m/rad), the core of the SRAM (3.93×10^{-10} N·m/rad), the yarn host of the HYAM (7.01×10^{-10} N·m/rad), and the guest of the HYAM (7.74×10^{-11} N·m/rad).

Using these experimental measurements of sheath and core properties, and the approximation that $d_{\text{core}}^{\text{Uncoated}} = d_{\text{core}}^{\text{on}}$ (and no fitted parameter), exceptional agreement was obtained between the predicted and observed dependence of torsional actuation on the sheath/core ratio (Fig. 2E). This theory predicts zero torsional stroke when the sheath/core ratio is infinite. In addition, there is an optimal value of the sheath/core ratio for maximizing torsional stroke.

6. Predicted tensile stroke and isobaric contractile work capacity of coiled SRAMs and HYAMs

While the calculations in this section pertain to any means of driving actuation, we here focus discussion on the specific case where actuation results from vapor absorption and desorption. The dependence of muscle stroke (ΔL) and contractile work capacity (W) on isobaric load (F) were calculated for both SRAMs and HYAMs from the force-extension curves shown in Fig. S21, which approximate that the helical springs in non-actuated and actuated states have strain-independent spring stiffnesses, K_{off} and K_{on} , respectively. The isobaric tensile stroke becomes

$$\Delta L = \delta_1 + \Delta L_0 - \delta_2 = \Delta L_0 - F(1/K_{\text{on}} - 1/K_{\text{off}}), \quad (6.1)$$

where $\delta_1 = F/K_{\text{off}}$ and $\delta_2 = F/K_{\text{on}}$. ΔL_0 is defined as the free tensile stroke, which is the stroke that would arise for a vanishing load if inter-coil contact did not occur. This free stroke would also be the observed stroke if the spring stiffnesses for the muscle were the same in the actuated and non-actuated states. When actuation takes place under isobaric load, the area enclosed by the rectangle ABCD in Fig. S21 provides the contractile work capacity, which is:

$$W = F\Delta L = F(\delta_1 + \Delta L_0 - \delta_2) = F\Delta L_0 - F^2(1/K_{\text{on}} - 1/K_{\text{off}}). \quad (6.2)$$

Equations 6.1 and 6.2 show that isobaric tensile stroke and contractile work capacity are determined by both the free stroke (ΔL_0) and the change in inverse stiffness ($1/K_{\text{on}} - 1/K_{\text{off}}$). However, these two terms provide opposite effects: contractile stroke ΔL_0 is produced when the muscle volume expands during activation to produce muscle untwist, while the change in inverse stiffness (from non-actuated to actuated state) leads to an extension of the spring when $K_{\text{on}} < K_{\text{off}}$, which is usually the case.

To complete the calculations, we next derive the free stroke ΔL_0 . Based on the twist-driven coil actuation mechanism (36), the free stroke is $\Delta L_0 = l^2 \Delta T / N$, where l is the fiber length making up the coil, ΔT is the fiber untwist (torsional actuation) due to guest volume expansion and modulus decrease, and N is the number of coils in the fiber length.

Using a theoretical framework that is similar to the one used here for non-coiled muscles, the torsional actuation stroke ΔT can be estimated as follows. In the case of a coiled SRAM, the torque on the CNT core is balanced by the external torque (TQ) needed to provide torsional tethering. In the non-actuated state,

$$TQ = k_{\text{core}}^{\text{off}}(\Delta T_0 + \Delta T_{\text{free,off}}), \quad (6.3)$$

where $k_{\text{core}}^{\text{off}}$ is the torsional stiffness of the core in the non-actuated state, and $\Delta T_{\text{free,off}}$ is the change in core twist due solely to the compression applied by the drying sheath. The corresponding parameters for the actuated state are $k_{\text{core}}^{\text{on}}$ and $\Delta T_{\text{free,on}}$. The torque balance equation in the actuated state is written as:

$$TQ = k_{\text{core}}^{\text{on}}(\Delta T_0 + \Delta T_{\text{free,on}} - \Delta T) - k_{\text{sheath}}^{\text{on}} \Delta T. \quad (6.4)$$

Combining Eqns. 6.3 and 6.4 gives

$$k_{\text{core}}^{\text{off}}(\Delta T_0 + \Delta T_{\text{free,off}}) = k_{\text{core}}^{\text{on}}(\Delta T_0 + \Delta T_{\text{free,on}} - \Delta T) - k_{\text{sheath}}^{\text{on}} \Delta T, \quad (6.5)$$

which provides the following for the torsional stroke of the SRAM:

$$\Delta T = [k_{\text{core}}^{\text{off}}(\Delta T_0 + \Delta T_{\text{free,off}}) + k_{\text{core}}^{\text{on}}(\Delta T_0 + \Delta T_{\text{free,on}})] / (k_{\text{core}}^{\text{on}} + k_{\text{sheath}}^{\text{on}}). \quad (6.6)$$

Using an essentially identical approach, the torsional stroke for the HYAM is:

$$\Delta T = [k_{\text{host}}^{\text{off}}(\Delta T_0 + \Delta T_{\text{free,off}}) + k_{\text{host}}^{\text{on}}(\Delta T_0 + \Delta T_{\text{free,on}})] / (k_{\text{host}}^{\text{on}} + k_{\text{guest}}^{\text{on}}), \quad (6.7)$$

where $k_{\text{host}}^{\text{off}}$ and $k_{\text{host}}^{\text{on}}$ are the torsional stiffnesses of the host yarn in the non-actuated and actuated state, respectively, and $k_{\text{guest}}^{\text{on}}$ is the torsional stiffnesses of the yarn sheath in the actuated state.

These calculations of torsional stroke for a coiled PEO-SO₃@CNT SRAM and a coiled PEO-SO₃@CNT HYAM use the same torsional stiffnesses as exploited in Section 5 for predicting the torsional stroke of a twisted SRAM and a twisted HYAM. The resulting ΔT is 0.17 turns/mm for the coiled SRAM and 0.11 turns/mm for the coiled HYAM.

We next predict the free tensile stroke (ΔL_0) for an ethanol-vapor-driven coiled PEO-SO₃@CNT SRAM and for an ethanol-vapor-driven coiled PEO-SO₃@CNT HYAM using the relationship that $\Delta L_0 = l^2 \Delta T / N$. For the investigated muscles, the number of coils (N) in the SRAM and in the HYAM were $N = 106$ and $N = 116$, respectively, and the fiber lengths within the coiled SRAM and HYAM were $l = 5.6$ cm and $l = 5.8$ cm, respectively. Using the ΔT values predicted using Eqns. 6.6 and 6.7 (0.17 and 0.11 turns/mm for the SRAM and HYAM, respectively), ΔL_0 becomes 5.1 mm and 3.1 mm for the SRAM and HYAM, respectively.

Using Eqns. 6.1 and 6.2, respectively, and the above values of ΔL_0 , provides the predicted dependence of tensile stroke and contractile work capacity on the applied isobaric stress. As shown in Fig. S22, the theoretically and experimentally obtained tensile stroke and work capacities are in exceptional agreement for stress levels that are sufficiently high that coil-coil contact does not limit actuation.

7. A SRAM-base knitted textile that changes porosity when exposed to water

Water-responsive twisted SRAM yarn muscles were also used to fabricate knitted textiles that respond to the presence of perspiration by opening pores. For making these SRAMs, a 1-mm-diameter aramid yarn core was twisted under 4 MPa stress (so that the total twist in the yarn was 16 turns/cm), and then the yarn was overcoated with a SRAM sheath (PEO-SO₃). This aramid yarn (PPTA, ST10M from Jiangsu Shino New Materials Technology Co.) contained thirty-seven, 53- μ m-diameter poly(p-phenylene terephthalamide) filaments in the yarn cross-section. While maintaining tension on the yarn to prevent coiling, a commercial sock-knitting machine (WH-6H-C from Huaxing Company) was used to make a weft-knitted textile sock from this homochiral SRAM, which is shown in Fig. S23 (left). Upon release of this tension, yarn twist was partially converted to yarn writhe (i.e., coiling), thereby resulting in a weft knitted sock that is shown in Fig. S23 (middle and right). As illustrated in Fig. S23, this coiling during stress release transformed the knitted sock into one in which opposite textile sides have quite different structures, and wherein the heads of the textile loops bridge the separation between textile sides. To understand the structure of the coiled SRAM fibers in the released textile, the textile structure was permanently set by coating the yarns in the textile with epoxy resin, then allowing the epoxy to cross-link. Removal of a set yarn from the textile showed that the yarn in the textile (Fig. S23C) had a coil index of 27.5.

Figure S24B shows the reversible actuation that occurs when the knitted SRAM textile was sprayed with water. Absorption of water caused the hole area of the textile to increase from 42.2% of the total textile area before water exposure to 60.8% after water exposure. The total area of the textile increased by about 28% and the average area between each of the loops increased by about 17%. This increased porosity resulted from yarn untwist to produce increased writhe. The increased writhe caused the textile to shear like an opening wine rack, thereby increasing porosity and decreasing the length in the warp direction by 18.6%, while maintaining the length in the weft direction.

8. A glucose-powered sheath run artificial muscle

Glucose-powered SRAMs that provide tensile actuation were made that exploit the same basic mechanism as previously used for torsional HYAMs (31) and shape-changing optical elements for optical glucose sensors (37). In this mechanism, phenylboronic acid is used as a substituent on a polymer chain within a polymer network. Reaction of these phenylboronic acid substituents with diols, in this case glucose, causes the phenylboronic acid to be progressively converted from neutral to charged. These charged species increase the hydrophilicity of the network, leading to polymer swelling by the incorporation of water, thereby enabling actuation.

A glucose-powered SRAM was fabricated using a commercial nylon thread (Coats & Clark, USA) as the core and a phenylboronic acid-containing polymer network (PA-BA) as the sheath. Acrylamide, 3-(acrylamido)phenylboronic acid, *N,N'*-methylenebis(acrylamide), dimethyl sulfoxide (DMSO), and D-(+)-glucose were purchased from Sigma-Aldrich. Irgacure I-369 photoinitiator (2-benzyl-2-(dimethylamino)-1-[4-(morpholinyl) phenyl]-1-butanone) was donated by BASF Corporation. All reagents were used as received. The sheath was formed on the nylon thread core by dip-coating monomer solution and subsequent UV-induced, free-radical polymerization, where I-369 serves as the photoinitiator and *N,N'*-methylenebis(acrylamide) serves as the crosslinker. The monomer solution contained acrylamide (78 mol%), 3-(acrylamido)phenylboronic acid (20 mol%), *N,N'*-methylenebis(acrylamide) (2 mol%) in DMSO. Additionally, I-369 was added at a concentration of 2 wt% of the total monomer content. The DMSO concentration in the final solution was 50 wt%. This monomer solution was coated on the nylon thread. Photopolymerization was initiated by irradiating the coated thread for 5 minutes with 365 nm UV light having an intensity of 250 mW/cm² (Lumen dynamics, OmniCure LX400+). About a 10-μm-thickness of sheath was formed by repeating this coating and photopolymerization process 3 times, which produced the twisted SRAM shown in Fig. S24A. After this process, a self-coiled PA-BA@nylon SRAM was made by inserting 38.4 turns/cm of twist while the thread was under an isobaric load of 7.3 MPa (Fig. S24B).

After 1 hour of immersion of the PA-BA@nylon SRAM in water, the glucose concentration was increased every 30 minutes, and the resulting equilibrium actuation was measured optically for each new glucose concentration. Figure S24C shows the tensile stroke of PA-BA@nylon SRAM as a function of glucose concentration in deionized water. When exposed to 100 mM glucose concentration, the PA-BA@nylon SRAM provided a tensile contraction of 1.12% while under 12.4 MPa isobaric load.

9. Additional possible applications of sheath run artificial muscle

Because of major performance improvements and radically decreased cost compared with the highest performance HYAMs, which presently use expensive CNT yarns, the application possibilities of SRAMs are diverse. They extend from microscale actuators that intelligently control flow in fluidic circuits to macroscale arrays of actuators for humanoid robots and exoskeletons.

The use of SRAMs for harvesting chemical or thermal energy as mechanical energy, which is then converted to electrical energy, is interesting for both small-scale and large-scale applications, like powering remotely communicating sensors and harvesting electrical energy from industrial waste streams. Twistron yarn harvesters can be connected in series with SRAMs to convert generated mechanical energy to electrical energy (27). The inherently higher mechanical power generation capabilities of SRAMs, compared with HYAMs, will provide a correspondingly higher electrical power output.

Applications in which artificial muscles intelligently actuate by sensing their environment are of great interest (29). Since SRAMs can provide intelligent actuation from cheap yarns, they are promising as yarns for comfort-adjusting and protective clothing, and for geotextiles that appropriately respond to environmental conditions to change porosity. Textile responses to ambient variables can be engineered by the design of textile structure and by using differing guest sheath compositions in multiple SRAMs or SRAM segments to provide either additive or subtractive responses to different environmental influences for driving actuation, like temperature, exposure to moisture (like sweat), and sunlight.

The increased sensitivity and response rate of SRAMs might eventually enable their use for detecting antigens in blood using sheaths of known antigen/antibody substituted polymers (30), which expand because of water absorption when a native antigen breaks cross-links between polymer chains. As one of many options, bio-responsive muscles could be used as the yarns of a braided cylinder (like in fig. S20), so that muscle contraction squeezes a pouch to release a drug. The presently demonstrated ability to eliminate CNTs from high performance artificial muscles might accelerate medical acceptance. In other applications, the SRAMs could be used to actuate valves that control the flow of liquids depending upon their chemical composition or temperature (or a combination of these effects, using mechanical logic circuits).

Figures, Tables, and Movie Captions

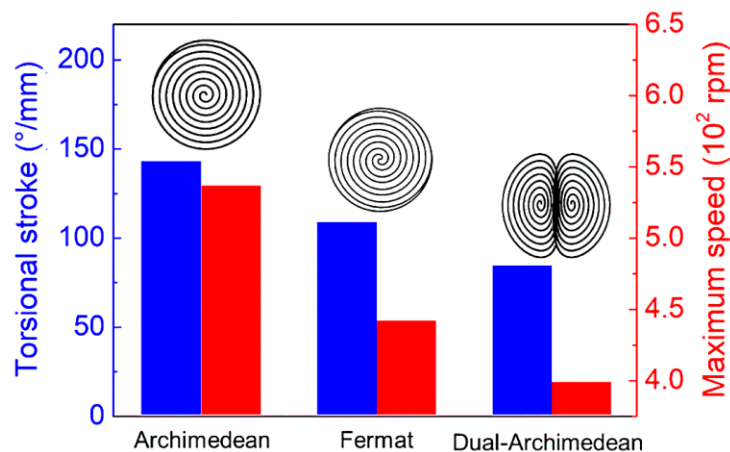


Fig. S1. The effect of yarn structure on the maximum torsional stroke and torsional rotation speed of a PEO-SO₃@CNT SRAM when driven by a saturated atmosphere of ethanol in dry air. These results are for three different scroll types: an Archimedean yarn (45- μ m-diameter, 74 turns/cm), a Fermat yarn (44- μ m-diameter, 69 turns/cm), and a dual-Archimedean yarn (49- μ m-diameter, 71 turns/cm). The applied load during twist insertion was 8 MPa.

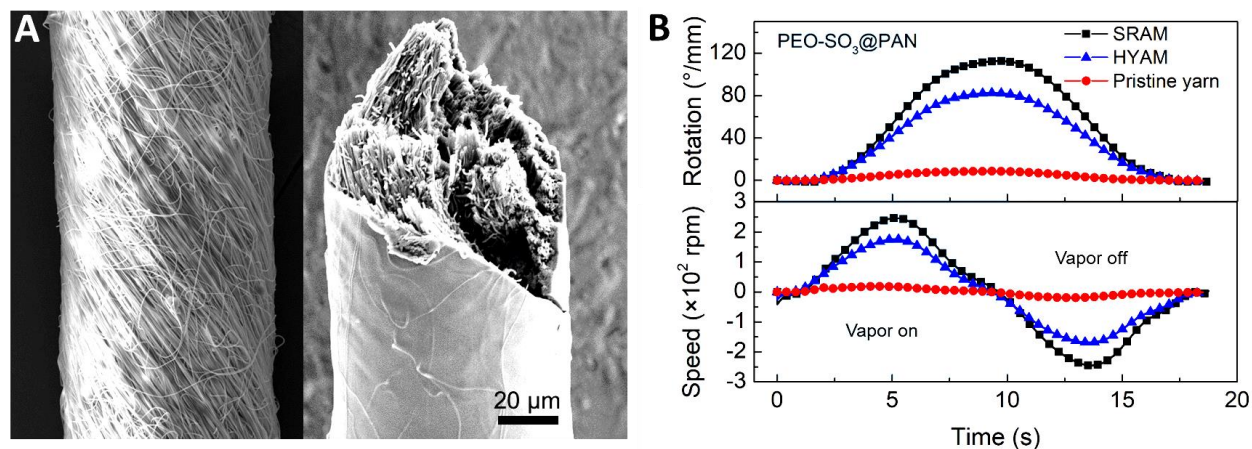


Fig. S2. SEM micrographs of: (A) A 76- μ m-diameter pristine yarn made from electrospun PAN nanofibers having an average diameter of 245 nm (left) and the fracture surface of an 87- μ m-diameter PEO-SO₃@PAN SRAM (sheath/core ratio of 0.073) that was made from the yarn in the left (right). The yarn was fracture by bending in liquid N₂. (B) The time dependence of torsional stroke and rotation speed for one reversible ethanol sorption/desorption cycle for an 87- μ m-diameter PEO-SO₃@PAN SRAM (black), a 92- μ m-diameter PEO-SO₃@PAN HYAM (blue), and a 76- μ m-diameter pristine yarn (red). The same 76- μ m-diameter PAN yarn, containing 23 turns/cm of twist, was used for the neat muscle and for the fabrication of the SRAM and HYAM. Also, the SRAM and HYAM had about the same weight (4.8 mg/cm). The PEO-SO₃@PAN SRAM of (B) has a sheath/core ratio of 0.073.

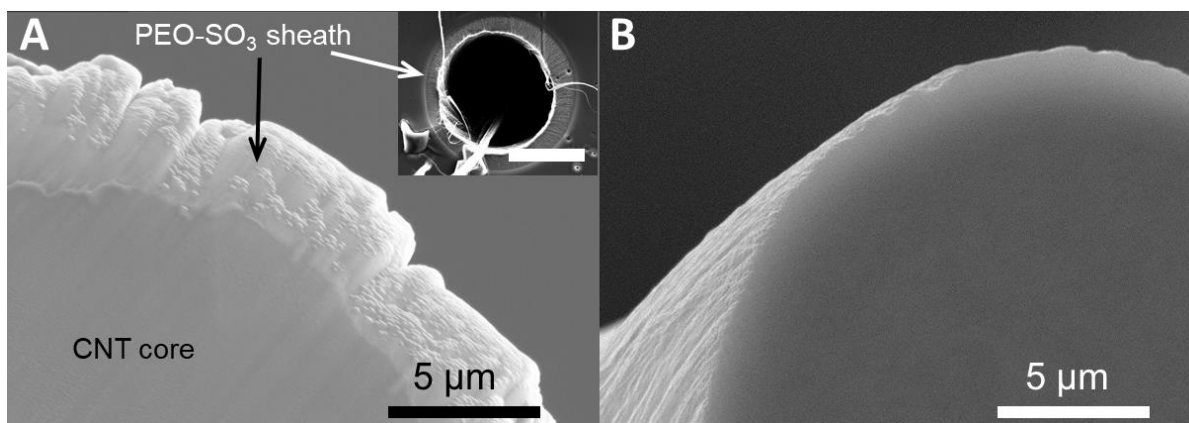


Fig. S3. SEM images of the cross-sections of (A) a PEO-SO₃@CNT SRAM (Inset: SEM micrograph of PEO-SO₃@CNT SRAM yarn after tensile rupture, which removed parts of the core yarn. The scale bar of the inset image is 20 μm) and (B) a PEO-SO₃@CNT HYAM, which were obtained by yarn sectioning using ion milling. The core CNT yarn in the SRAM has a diameter of 37 μm, and the PEO-SO₃ polymer sheath is about 5 μm thick.

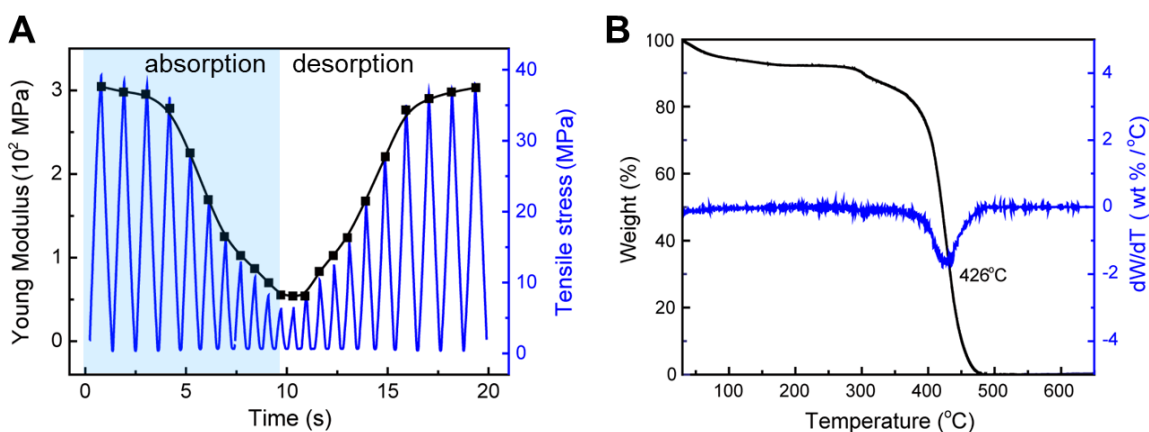


Fig. S4. (A) Young's modulus as a function of time during the sorption and desorption of ethanol by a freestanding, 137-μm-thick PEO-SO₃ film. This modulus (black line and data points) was obtained by the pictured cycling to 7% strain at 0.8 Hz (blue line). Ethanol sorption (using a saturated atmosphere of ethanol in dry air) was continued until the modulus became essentially constant (at about 10 s, where the film weight had increased by 16.3%), which resulted in the pictured change in tensile stress. Thereafter, desorption of ethanol occurred in dry air using the same gas flow as for ethanol sorption. (B) Thermal gravimetric analyses of the PEO-SO₃ film at a heating rate of 5°C/min in air.

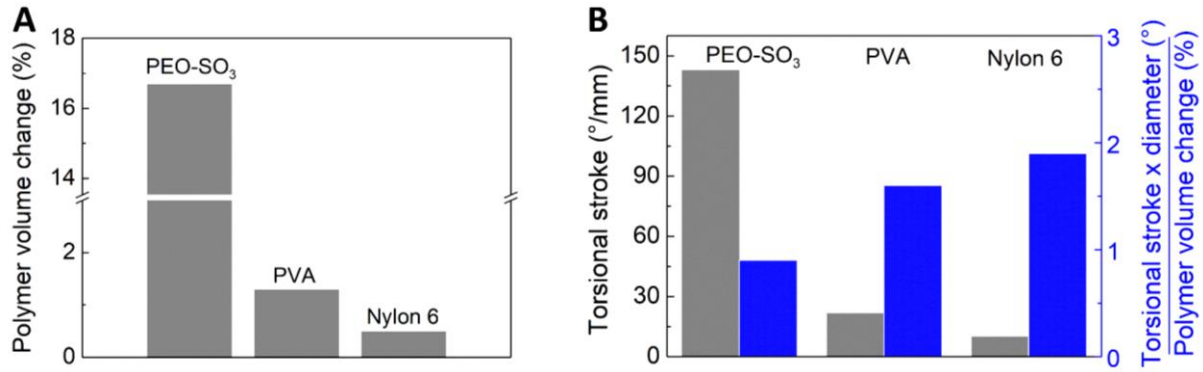


Fig. S5. (A) The equilibrium volume change of PEO-SO₃, PVA, and nylon 6 films when exposed to a saturated atmosphere of ethanol in dry air. (B) Comparison of equilibrium torsional strokes for an applied stress of 33 kPa (and the product of torsional stroke and core yarn diameter, normalized to the percent polymer volume change) for a 37.5- μ m-diameter, non-coiled CNT yarn (twist density = 74 turns/cm) that is coated with either PEO-SO₃, PVA, or nylon 6, using the same vapor delivery conditions as in (A). These torsional strokes resulted from exposure of the SRAMs to a saturated atmosphere of ethanol in dry air. The sheath/core ratios for the PEO-SO₃@CNT, PVA@CNT, and nylon6@CNT SRAMs were 0.14, 0.17, and 0.12, respectively.

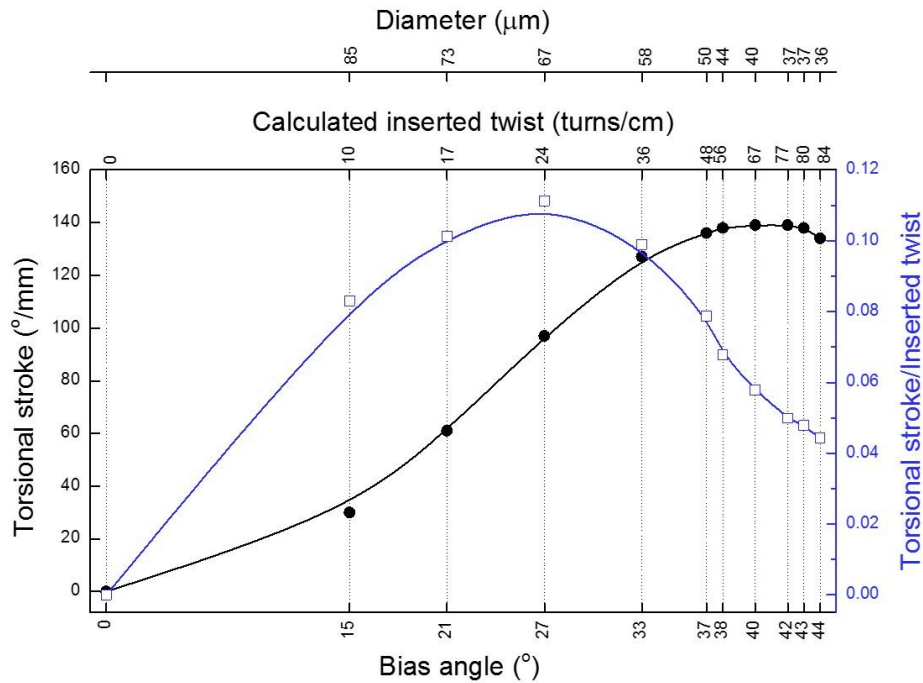


Fig. S6. The dependence of torsional stroke on the measured bias angle (α) of a CNT core yarn on a linear scale (before sheath deposition) for a twisted PEO-SO₃@CNT SRAM. These torsional strokes are equilibrium values for a SRAM exposed to a saturated atmosphere of ethanol in dry air. The lower-top axis is the inserted twist per yarn length (T), which is calculated using the bias angle of the core yarn (α) and the yarn diameter (D , which is provided by the upper-top axis) using $T = \tan(\alpha)/\pi D$. Yarn coiling does not initiate until the bias angle exceeds 43.4°, at which point the diameter of the CNT yarn is 36.5 μ m. After overcoating with PEO-SO₃, this diameter yarn provides a SRAM having a sheath/core ratio of 0.14.

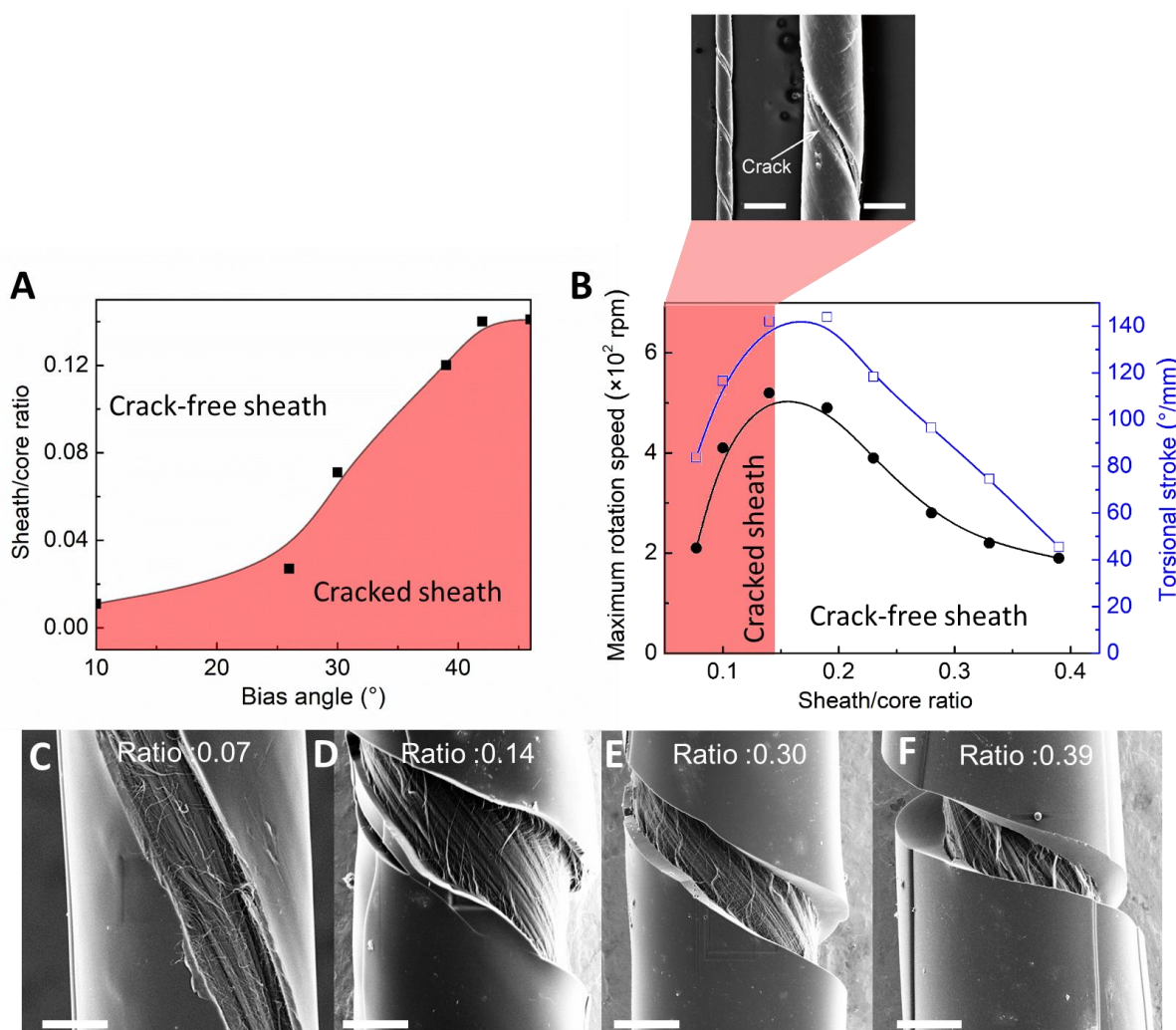


Fig. S7. Effects of sheath/core ratio on the fabricability and performance of a PEO-SO₃@CNT SRAM. (A) Combinations of sheath/core ratio and yarn bias angle (prior to sheath coating) that result in sheath cracking (red region) during SRAM fabrication and combinations that result in crack-free sheaths (white region). (B) For actuation by a saturated atmosphere of ethanol in dry air, the dependence of torsional stroke and maximum rotation speed on sheath/core ratio for a non-coiled 39- μ m-diameter PEO-SO₃@CNT SRAM containing 74 turns/cm of twist, which had a bias angle of 42° before sheath coating. Inset: SEM micrographs at two magnifications showing the sheath cracking that occurs for sheath/core ratios that are in the red-colored region of the data plot. The scale bars are 150 μ m (left) and 30 μ m (right). (C-F) SEM micrographs showing the sheath-core structure of PEO-SO₃@CNT SRAMs having progressively higher sheath-core ratios. The muscle sheath was intentionally cracked by untwisting the muscle while it was immersed in liquid nitrogen. The scale bars are 20 μ m.

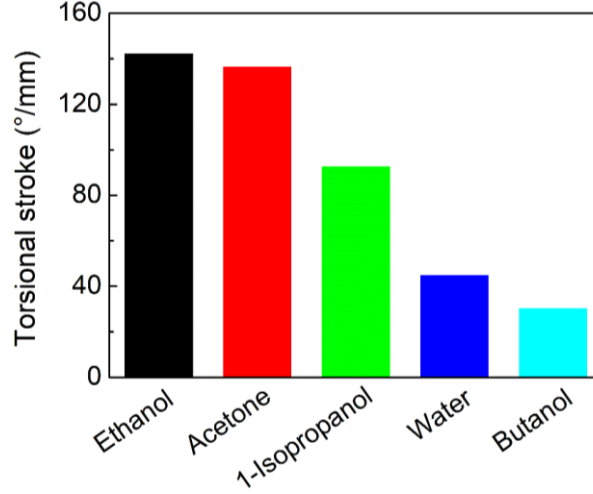


Fig. S8. Equilibrium vapor-driven torsional stroke (using vapor-saturated dry air) of a twisted PEO-SO₃@CNT SRAM under 0.1 MPa tensile stress. This SRAM is the same as used for Fig. 2B and D.

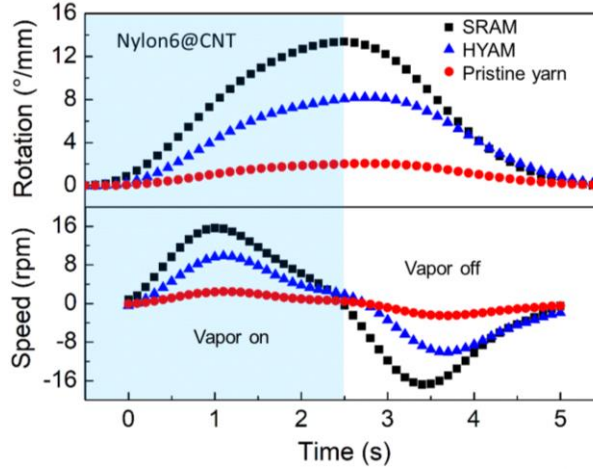


Fig. S9. The time-dependence of torsional stroke and torsional rotation speed for water-vapor-driven actuation of a 44- μ m-diameter nylon6@CNT SRAM, a 47- μ m-diameter nylon6@CNT HYAM, and a 39- μ m-diameter pristine CNT yarn, which was obtained by switching between 45% RH air and 90% RH air. All yarns contain the same weight of CNTs, and both nylon6@CNT muscles have similar linear densities (0.29 mg/cm). The applied tensile stress for these experiments was 0.35 MPa. The twist densities of the SRAM, the HYAM, and the pristine yarn are 72 turns/cm.

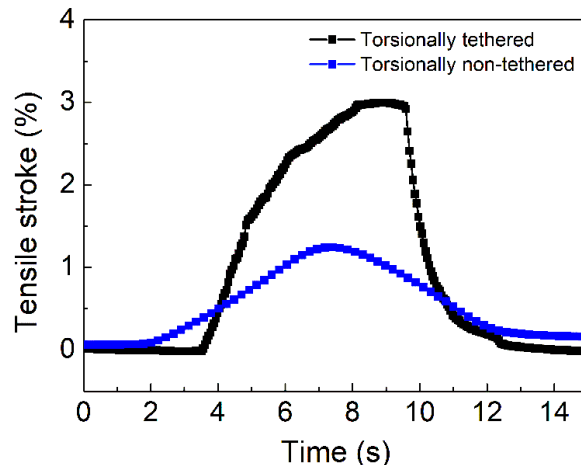


Fig. S10. Comparison of the time-dependence of tensile stroke for a torsionally tethered and a torsionally non-tethered twisted PEO-SO₃@CNT SRAM, when muscle contraction resulted from exposure of the muscles to a saturated atmosphere of ethanol in dry air and actuation was reversed by desorbing the ethanol using dynamic pumping. These measurements (for a tensile load of 0.1 MPa) are for the same SRAM as used in Fig. 2B and C.

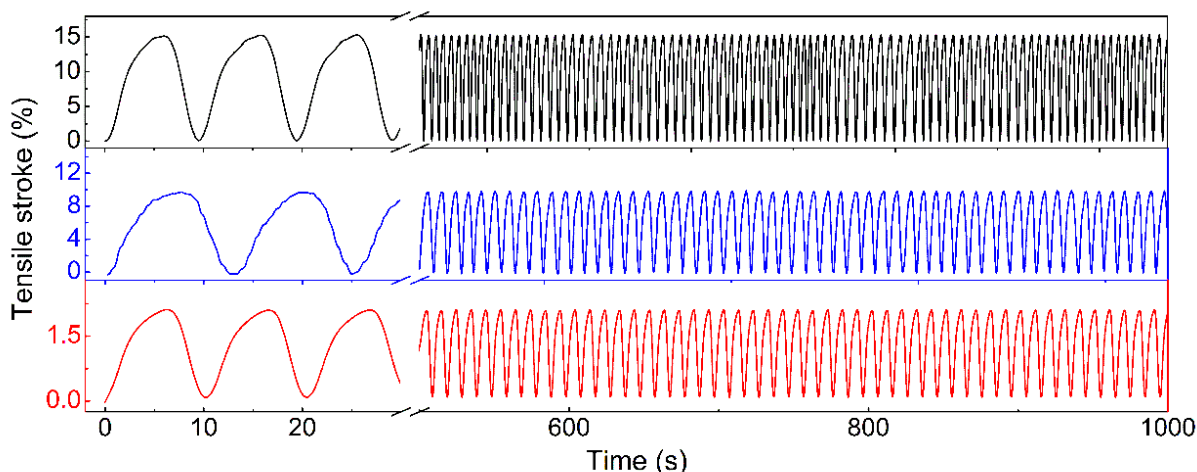


Fig. S11. Tensile stroke versus time for a coiled PEO-SO₃@CNT SRAM (top), a coiled PEO-SO₃@CNT HYAM (middle), and a coiled pristine yarn (bottom). Actuation cycles were obtained by exposing the muscles to dry air containing 0.17 mg/L of ethanol and then desorbing the ethanol using dynamic pumping. Before coiling, the diameters of the SRAM, the HYAM, and the pristine yarn were 43, 47, and 38 μ m, respectively. The applied stress during coiling and during actuation were 8 MPa and 33 MPa, respectively. All muscles contained the same weight of CNTs per untwisted length, and both PEO-SO₃@CNT muscles have similar linear densities (0.33 mg/cm before coiling). The spring indexes of the SRAM, the HYAM, and the pristine yarn were 0.51, 0.56, and 0.32, respectively.

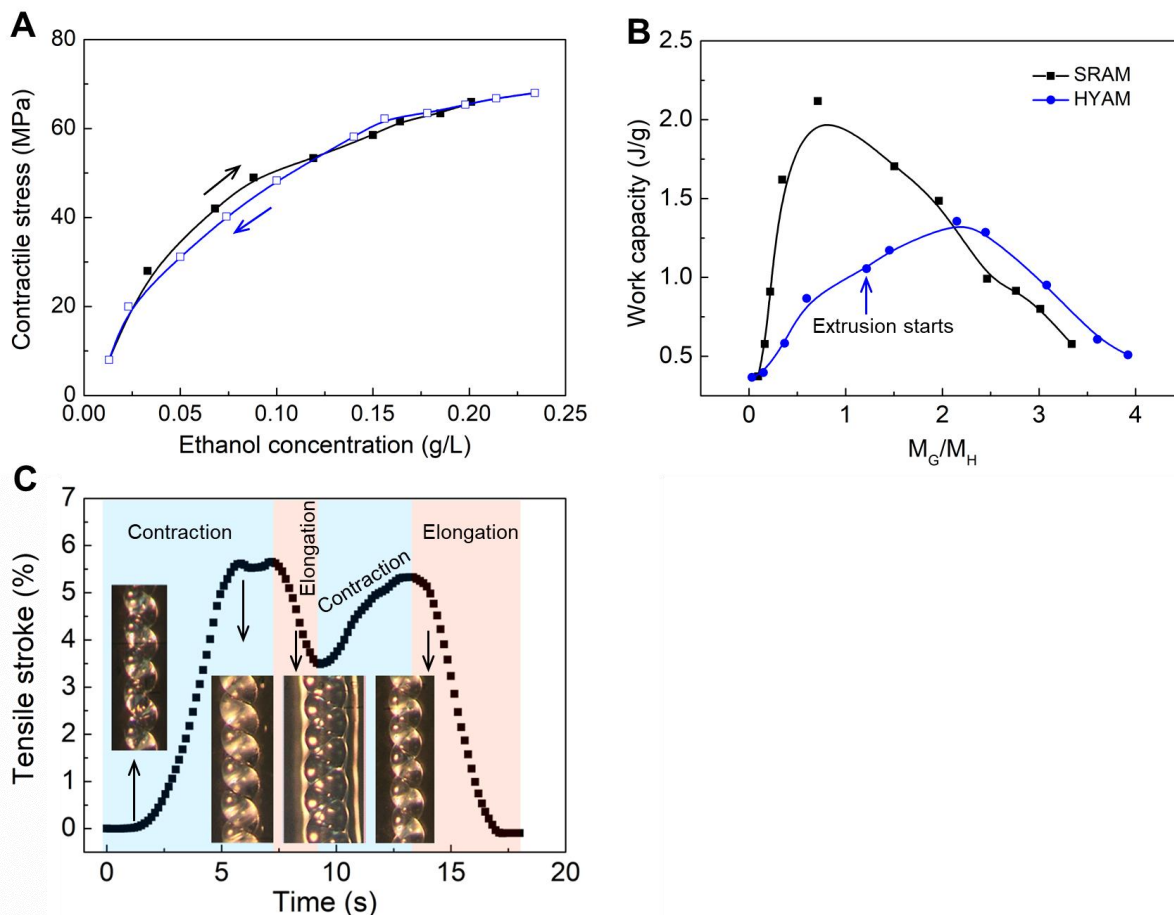


Fig. S12. (A) Equilibrium tensile stress generation as a function of ethanol concentration in dry air for isometric tensile actuation of a coiled PEO-SO₃@CNT SRAM. The outer diameter of the self-coiled SRAM was 44 μm , its inserted twist was 110 turns/cm, and its sheath/core ratio was 0.14. (B) Load-optimized work capacity of a coiled PEO-SO₃@CNT SRAM and HYAM as a function of guest-to-host mass ratio (M_G/M_H). The mass ratio at which the guest PEO-SO₃ begins to extrude from the HYAM during coiling is indicated. (C) The effect of using an overly thick sheath on the actuation of a SRAM when the applied mechanical load is low (3.1 MPa). Actuation was produced by dropwise addition of ethanol to a PEO-SO₃@PU SRAM that had a sheath-core ratio of 2.27. The insets are optical microscope images during the contraction and expansion processes.

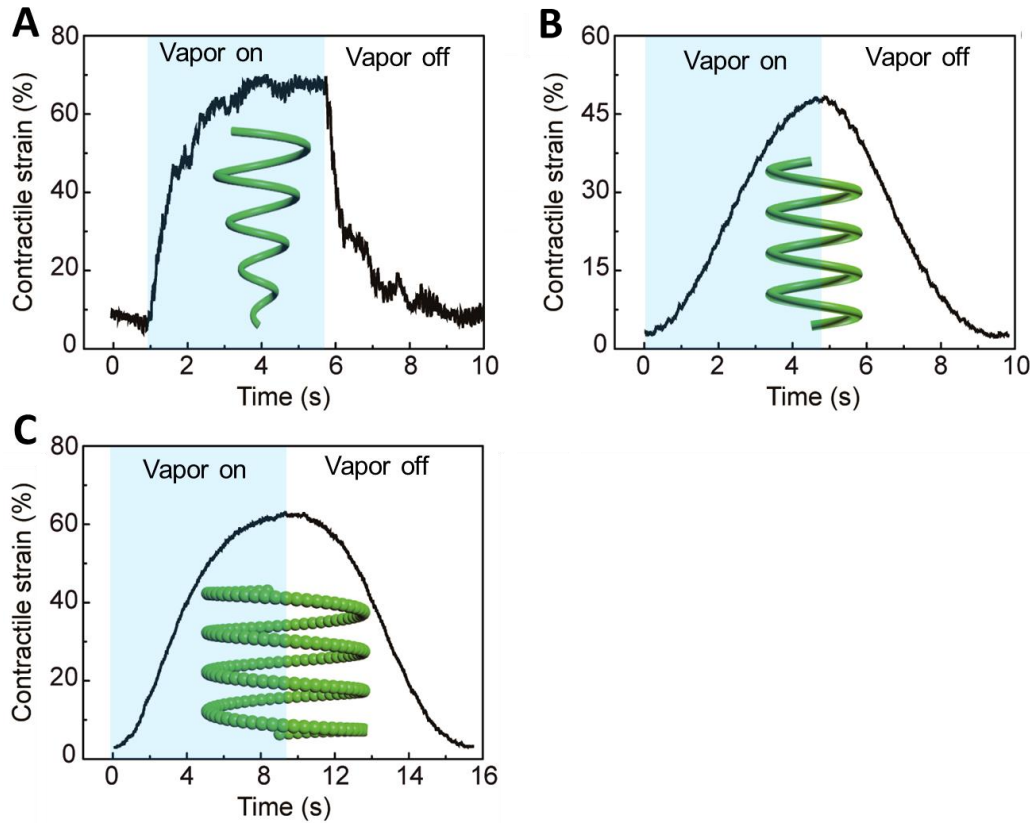


Fig. S13. Humidity-driven tensile actuation (during transition from 55% to 90% RH air) versus time for PEO-SO₃@CNT SRAMs having a sheath/core ratio of 0.14, which were made from a precursor 44- μ m-diameter twisted SRAM having 72 turns/cm of twist. Tensile stroke versus time is shown for (A) a twisted SRAM that was coiled on a 0.35-cm-diameter, 1.2-cm-long cone-shaped mandrel, thereby forming a non-uniformly coiled SRAM. (B) A twisted SRAM that was coiled on a 0.2-cm-diameter, 1-cm-long cylindrical mandrel, thereby forming a uniformly coiled SRAM. (C) A self-coiled SRAM that was coiled on a 0.2-cm-diameter, 0.5-cm-long cylindrical mandrel, thereby forming a supercoiled SRAM. The applied tensile stresses for these experiments were 0.5 MPa, 0.5 MPa, and 0.7 MPa, respectively. Insets: The structures of these muscles are illustrated in (A-C).

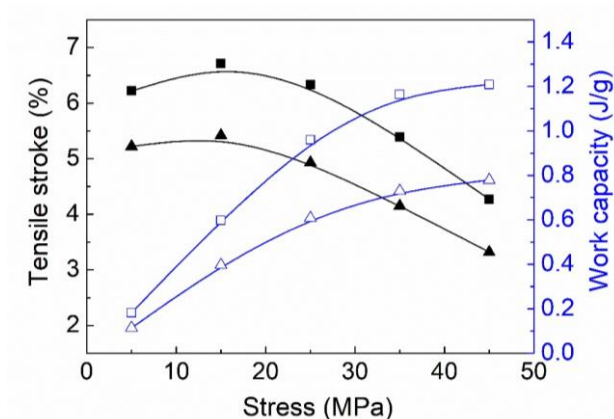


Fig. S14. Comparison of the dependence of equilibrium tensile stroke and contractile work capacity on applied isobaric stress for a coiled PEO-SO₃@CNT SRAM (squares) and a coiled PEO-SO₃@CNT HYAM (triangles) for a temperature increase from 25°C to 200°C at 5°C/minute in a TMA. Before coiling, the diameters of the SRAM and the HYAM yarn were 44 and 47 μm , respectively, and the spring indices after coiling were 0.51 and 0.56 for the SRAM and HYAM, respectively. The sheath/core ratio of the SRAM was 0.14.

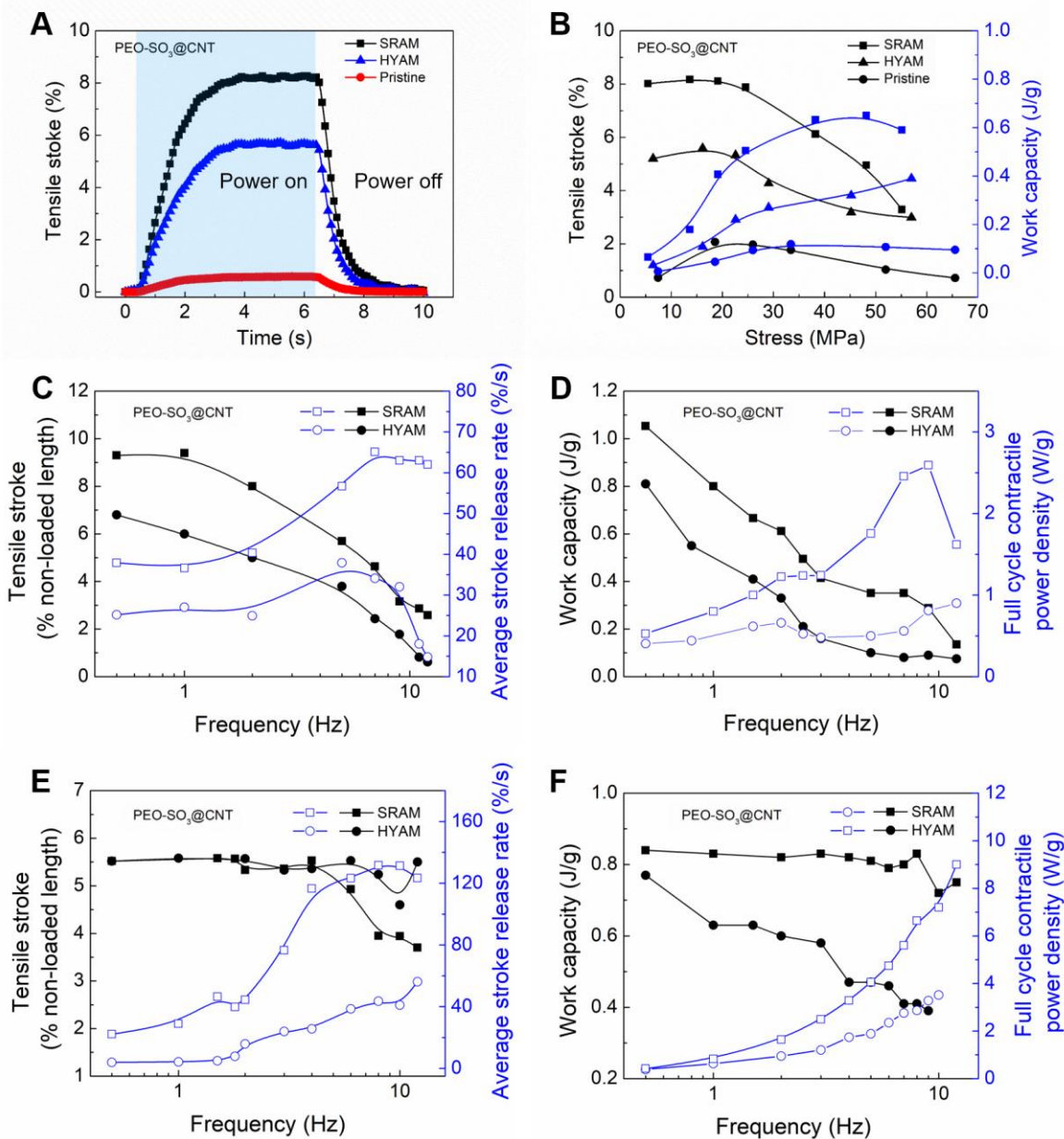


Fig. S15. Comparison of electrothermally-powered tensile actuation for a coiled SRAM, a coiled HYAM, and a coiled pristine yarn. (A) Tensile stroke versus time for a PEO-SO₃@CNT SRAM, a PEO-SO₃@CNT HYAM, and a pristine CNT yarn when electrothermally actuated using the isobaric load that maximized muscle stroke (18, 15, and 19 MPa, respectively). The input power per yarn length was 0.18 W/cm and a 0.08 Hz square-wave potential was applied, which provided peak temperatures of 167, 175, 190°C, respectively. Before coiling, the diameters of the SRAM, the HYAM, and the pristine yarn were 44, 47, and 36 μ m, respectively. (B) Equilibrium tensile stroke and contractile work capacity versus applied isobaric stress for the PEO-SO₃@CNT SRAM, the PEO-SO₃@CNT HYAM, and the pristine CNT yarn of (A), when using the same electrothermal heating conditions as in (A). The frequency dependence of (C) the tensile stroke and average tensile stroke release rate and (D) the per-cycle contractile work capacity and the full-cycle contractile power density for the PEO-SO₃@CNT SRAM and the

PEO-SO₃@CNT HYAM when driven in air by square-wave voltages between 0 and 12 V. The frequency dependence of (E) the tensile stroke and average tensile stroke release rate and (F) the per-cycle contractile work capacity and the full-cycle contractile power density for the PEO-SO₃@CNT SRAM and the PEO-SO₃@CNT HYAM when driven in a room-temperature water bath by square-wave voltages between 0 and 23 V. For (C), (D), (E), and (F), the diameters of the SRAM and the HYAM were 53 and 57 μm , and the load applied was around 29 MPa.

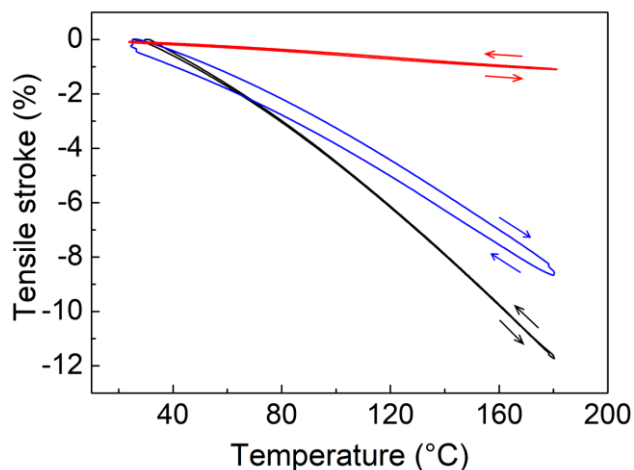


Fig. S16. Tensile stroke versus temperature (for increasing and decreasing temperature) for a nylon6@CNT SRAM (black line), a nylon6@CNT HYAM (blue line), and a pristine CNT yarn (red line). The same 39- μm -diameter CNT yarn was used for these experiments, and the weight of nylon 6 per muscle length was the same for the SRAM and for the HYAM. The sheath/core ratio of the SRAM was 0.12. The spring indices after coiling were 0.79, 0.86, and 0.63 for the SRAM, HYAM, and pristine yarn respectively. The applied tensile load for these experiments was 16.9 MPa.

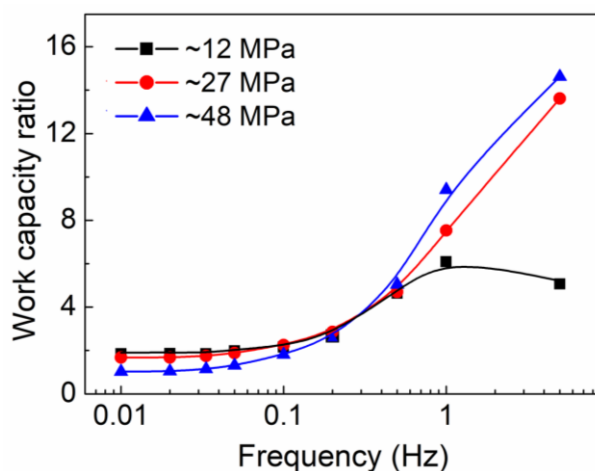


Fig. S17. Comparison of electrochemical tensile work capacity of a coiled CNT@nylon6 SRAM and a coiled CNT HYAM yarns in 0.2 M TBA-PF₆/PC electrolyte for square-wave-driven actuation between 0 and -3V. The frequency dependence of the ratio of SRAM work capacity to HYAM work capacity is shown, which was obtained from the data of Fig. 4D.

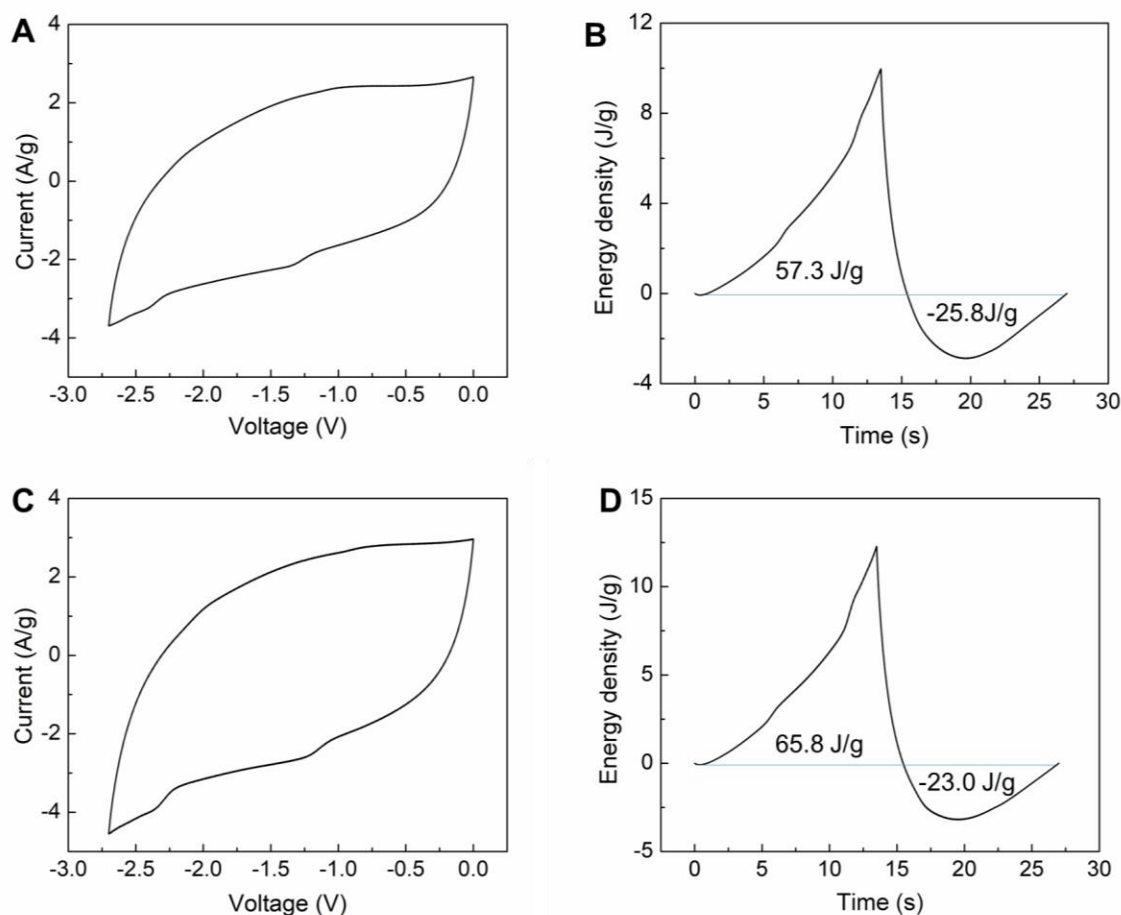


Fig. S18. Cyclic voltammetry scans and corresponding input and output electrical energies during electrochemical actuation of a CNT@nylon6 yarn and a pristine CNT yarn in 0.2 M TBA·PF₆/PC electrolyte at a scan rate of 200 mV/s. (A) A cyclic voltammetry scan and (B) the corresponding input and output electrical energies for a CNT@nylon6 yarn. (C) A cyclic voltammetry scan and (D) the corresponding input and output electrical energies for a pristine CNT yarn. These results were used to derive the contractile energy conversion efficiencies of electrochemical tensile actuation. The applied tensile stress for these measurements was ~30 MPa.

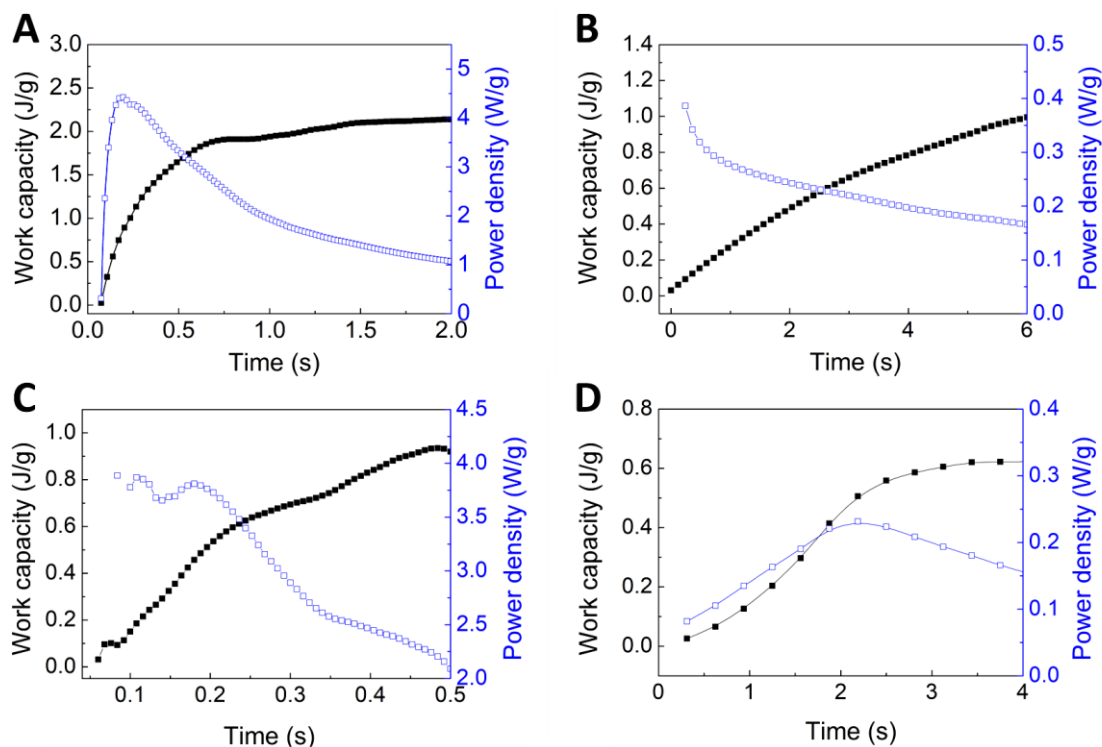


Fig. S19. Work capacity and maximum average contractile power, which is defined as the maximum ratio of contractile work to actuation time. These results are for the tensile load that maximizes contractile work. (A) Results for the ethanol-vapor-driven PEO-SO₃@CNT SRAM of Fig. 3A and a tensile load of 48 MPa. **(B)** Results for the electro-thermally-driven PU@CNT SRAM of Fig. 3C and a tensile load of 57 MPa. **(C)** Results for the electro-chemically-driven CNT@nylon6 SRAM of Fig. 4D and a tensile load of 48 MPa. Actuation resulted from switching the inter-electrode voltage from 0 V to -3V. **(D)** Results for the electro-thermally-driven PEO-SO₃@CNT SRAM of Fig. S15A and a tensile load of 48 MPa.

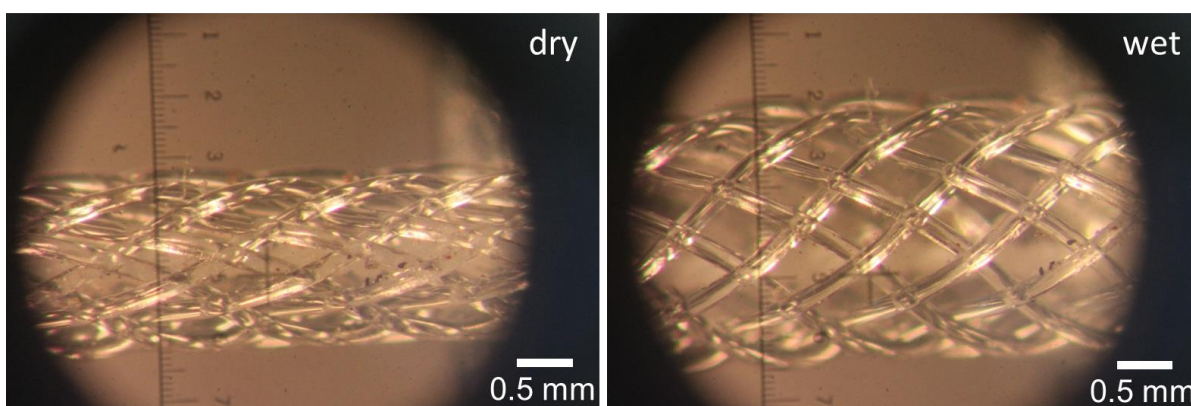


Fig. S20. Optical microscope image of a smart structure driven by a water-responsive, coiled PEO-SO₃@bamboo SRAM (200 μ m diameter with 0.32 sheath/core ratio), which is inside a 1.8-mm-diameter rope of 16 braided, 180- μ m-diameter nylon 6 fibers. Water absorption causes the SRAM, which is attached to braid ends, to contract, and the resulting decrease in braid length increases braid porosity.

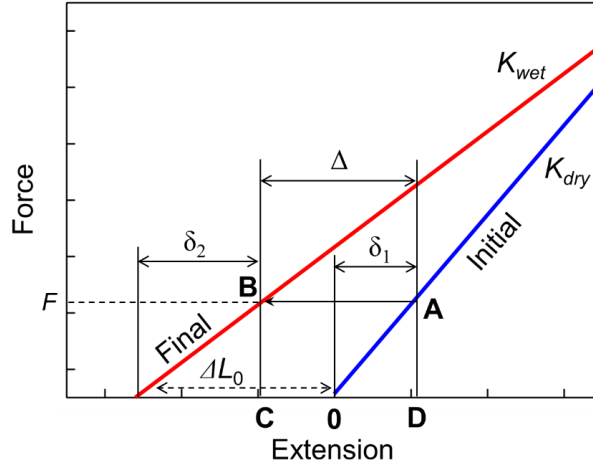


Fig. S21. Schematic illustration of the dependence of force on extension for actuated and non-actuated coils, which is used for the calculation of the load dependence of muscle stroke and contractile work capacity. This calculation uses the approximation that the stiffness of the muscle coil is strain independent for both non-actuated (dry) and actuated (wet) states. The symbols in this illustration are defined in Section 6.

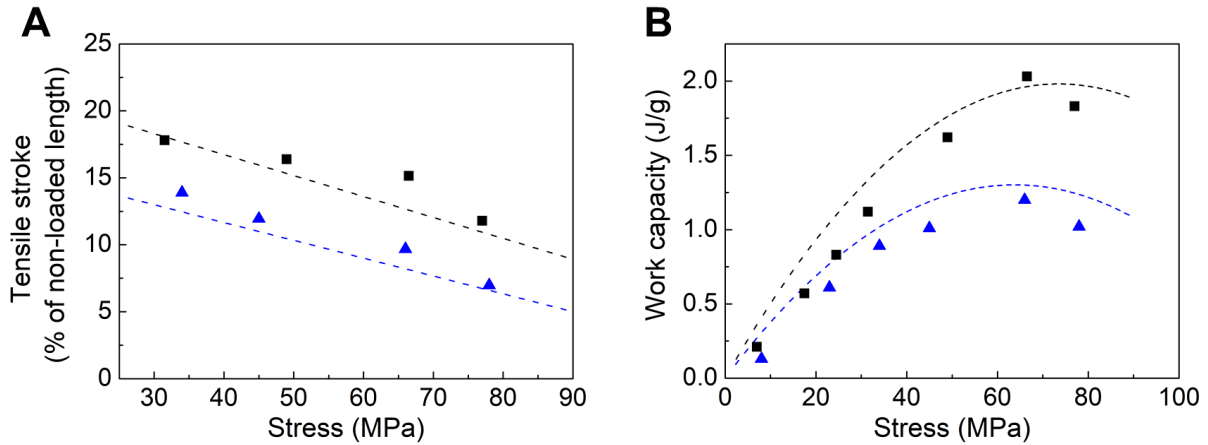


Fig. S22. Comparison of theoretical and experimental results for equilibrium ethanol-vapor-driven actuation of a PEO-SO₃@CNT SRAM and a PEO-SO₃@CNT HYAM. (A) Comparison of the stress dependence of the theoretically calculated and measured tensile stroke for a PEO-SO₃@CNT SRAM (dashed black line and black squares, respectively) and a PEO-SO₃@CNT HYAM (dashed blue line and blue triangles, respectively). (B) Comparison of the stress dependence of theoretically calculated and measured work capacity for a PEO-SO₃@CNT SRAM (dashed black line and black squares, respectively) and a PEO-SO₃@CNT HYAM (dashed blue line and blue triangles, respectively). This remarkable agreement between theoretical and experimental results was obtained without the use of any fitted parameter.

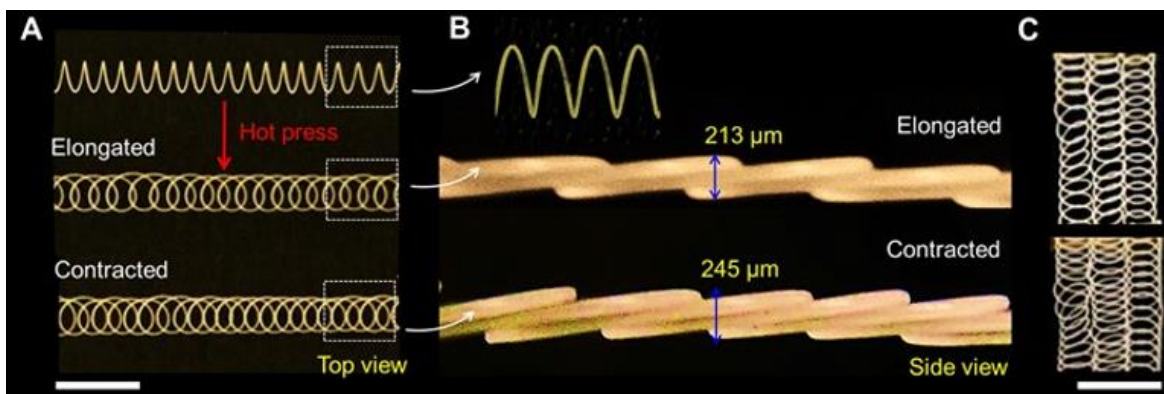


Fig. S23 Collapsed-helix SRAMs and their use as moisture-responsive fibers and textiles. (A) Photographs showing the fabrication of a planar SRAM: (top) A homochiral, mandrel-coiled, twisted SRAM using a 150- μm -diameter PEO-SO₃@polycarbonate yarn having a sheath/core ratio of 0.33, an inserted twist of 22 turns/cm, and a spring index of 11.5. Pressing this mandrel-coiled SRAM between flat plates at 120°C for 6 hours produced the below SRAM, which is pictured in initial (elongated) and moisture-actuated (contracted) states when the applied load is 4.3 MPa. (B) Orthogonal lateral views of the SRAMs in (A). (C) For illustrating the possible use of planar heterochiral SRAM in an intelligent textile, photographs of three SRAMs interconnected by an inert 150- μm -diameter fiber are shown for the expanded moisture-free state (top) and the contracted moisture-absorbed state (bottom). For an isobaric 4.7 MPa load, 48.6% contraction was obtained by exposing a homochiral planar SRAM to moist air (RH = 70%) after it had been equilibrated in an ambient RH of 34%. The scale bars for (A) and (C) are 1.5 and 1.8 cm, respectively. For clarity, the muscle backgrounds were made black.

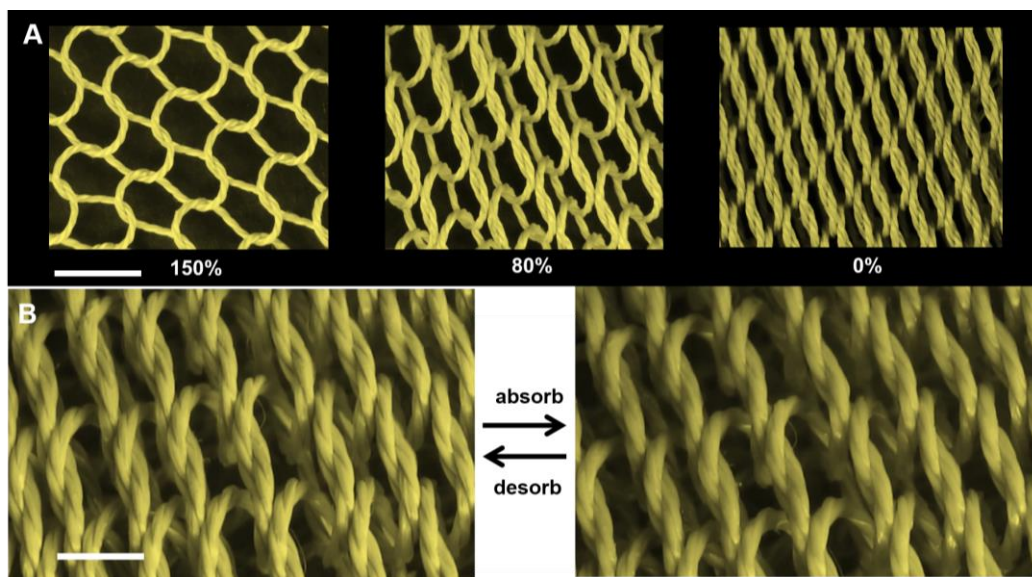


Fig. S24. Actuating textiles based on water-driven SRAMs. (A) Photographs of a sock that was weft-knitted from a PEO-SO₃@PPTA SRAM, where PPTA is poly(p-phenylene terephthalamide) yarn. As originally knitted (left), the sock was stretched by 150% along the sock axis (the vertical direction) and the sock diameter was held constant. Relaxing the axial direction strain to 80% and to 0% (keeping the sock diameter constant) caused the knitted structure to morph, as the twist of the SRAM was partially converted to coiling. Figure S25

shows other views of the strain-released textile. (B) Photographs showing the additional morphing during water absorption (to increase porosity) and desorption (to decrease porosity) for a dimensionally-unconstrained textile cut from the sock. The scale bars for (A), and (B) are 0.4, and 0.25 cm, respectively. For clarity, the muscle backgrounds in (A) and (B) were made black.

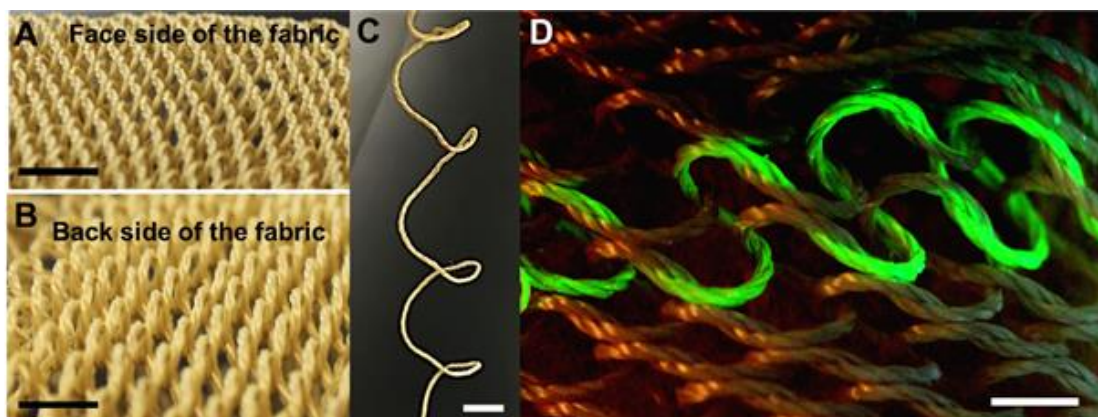


Fig. S25 Further description of the morphing SRAM structure shown in Fig. 24 A, B. (A, B) Photographs showing the differing structures on opposite sides of the knitted sock when the strain in the sock axis direction was completely released. (C) Photograph of a resin-set SRAM yarn extracted from the structure shown in A and B. (D) Photograph taken under UV light, in which the configuration of a single, fluorescently-dyed SRAM yarn can be seen in the face side of strain-released textile of (A, B). The scale bars for (A), (B), (C) and (D) are 0.5, 0.5, 0.8 and 1.5 cm, respectively.

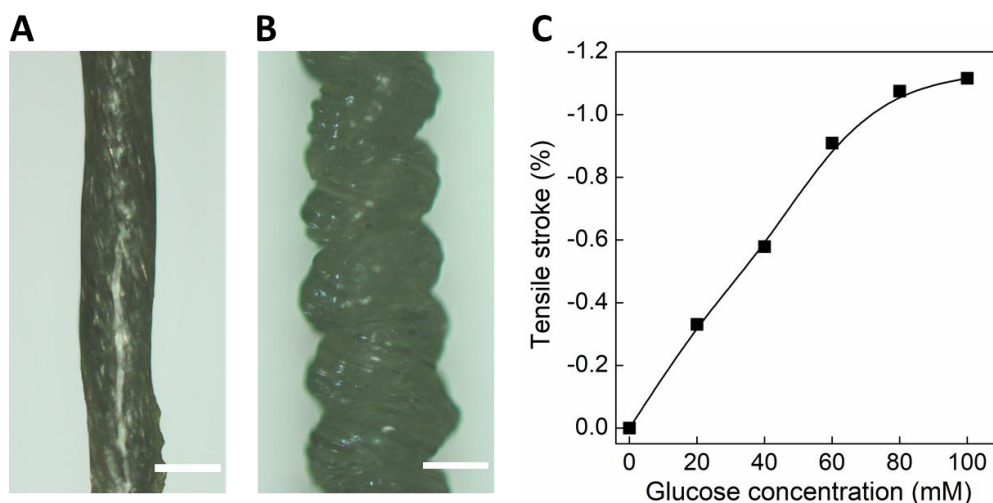


Fig. S26. Bio-SRAM driven by glucose. (A, B) Optical images of a nylon thread coated with a polyacrylamide polymer network having phenylboronic acid side chains before (A) and after (B) twist insertion to produce coiling. The scale bar is 200 μm . (C) Tensile actuation of bio-SRAM in response to glucose concentration while under isobaric load (12.4 MPa).

Table S1. Yarn source, initial yarn diameter, and number of fibers in yarn cross-section.

Yarn type and origin	Initial yarn diameter (μm)	Fiber diameter (μm)	Number of fibers in yarn cross-section
PAN nanofiber yarn (electrospun)	76	0.25	304
Silk yarn (Sulky of America)	56	1.5	33
Bamboo yarn (Weifang Meihua Textile Co. Ltd.)	235	20	8
Nylon 6 yarn (made at Donghua University)	60	15	3

Table S2. Contractile work densities (J/g) and maximum average-power densities (W/g) of a SRAM divided by that of a HYAM as a function of the applied stress. Bold numbers for these performance figures indicate that they are maximized at the listed applied stress.

Type of coiled muscle (muscle drive method)	PEO-SO ₃ @CNT (ethanol-vapor-driven) (Fig. 3B)	PEO-SO ₃ @CNT (electrothermally-driven) (Fig. S15B)	PU@CNT (electrothermally-driven) (Fig. 3D)	CNT@nylon vs. CNT (electrochemically-driven)
				Potential switched between 0 to -3V at 1 Hz (Fig. 4D and Fig. S17)
Contractile work density (J/g) of a SRAM divided by that of a HYAM as a function of the applied stress		0.18/0.09 = 2.00 @ 13.6 MPa	0.30/0.22 = 1.36 @ 17.0 MPa	0.41/0.068 = 6.03 @ 12 MPa, 15 MPa (load for SRAM and HYAM, respectively)
	0.56/0.47 = 1.19 @ 17.5 MPa	0.41/0.18 = 2.28 @ 19.0 MPa	0.53/0.28 = 1.89 @ 24.0 MPa	0.81/ 0.11 = 7.36 @ 27 MPa, 29 MPa
	0.81/0.66 = 1.23 @ 24.5 MPa	0.51/0.24 = 2.13 @ 24.0 MPa	0.79/0.38 = 2.08 @ 33.0 MPa	0.99 /0.10 = 9.9 @ 48 MPa, 42 MPa
	1.12/0.87 = 1.29 @ 33.0 MPa	0.63/0.30 = 2.10 @ 38.0 MPa	1.12/0.49 = 2.29 @ 42.0 MPa	
	1.61/ 1.15 = 1.40 @ 48.0 MPa	0.64 /0.34 = 1.88 @ 48.0 MPa	1.18/0.51 = 2.31 @ 49.0 MPa	
	2.12 /1.01 = 2.10 @ 66.0 MPa	0.59/ 0.37 = 1.59 @ 55.0 MPa	1.33 / 0.62 = 2.15 @ 57.0 MPa	
Maximum average power density (W/g) of a SRAM divided by that of a HYAM as a function of the applied stress		0.06/0.03 = 2.00 @ 13.6 MPa	0.06/0.05 = 1.20 @ 17.0 MPa	0.75/0.27 = 2.78 @ 12 MPa, 15 MPa
	1.23/0.62 = 1.98 @ 17.5 MPa	0.14/0.06 = 2.33 @ 19.0 MPa	0.106/0.065 = 1.63 @ 24.0 MPa	1.93/0.36 = 5.36 @ 27 MPa, 29 MPa
	1.77/0.87 = 2.03 @ 24.5 MPa	0.17/0.08 = 2.13 @ 24.0 MPa	0.16/0.088 = 1.82 @ 35.0 MPa	3.71 / 0.65 = 5.71 @ 48 MPa, 42 MPa
	2.45/1.15 = 2.13 @ 33.0 MPa	0.21/0.10 = 1.91 @ 38.0 MPa	0.26/0.11 = 2.36 @ 42.0 MPa	
	3.52/ 1.51 = 2.33 @ 48.0 MPa	0.22 /0.11 = 2.00 @ 48.0 MPa	0.35/0.18 = 1.94 @ 49.0 MPa	
	4.44 /1.30 = 3.42 @ 66.0 MPa	0.20/ 0.13 = 1.54 @ 55.0 MPa	0.37 / 0.18 = 2.06 @ 57.0 MPa	

Movie S1: Real time movie of the dimensional changes of a coiled PEO-SO₃@CNT sheath-run artificial muscle during actuation driven at ~0.1 Hz by the sorption and desorption of an equilibrium concentration of ethanol vapor in dry air. The muscle stroke, when lifting a 32 MPa load, was 8.5%.

Movie S2: Real time movie of the electrothermal actuation of a 2.6-cm-long, coiled PEO-SO₃@CNT sheath-run artificial muscle at 12 Hz in a room-temperature water bath. The actuator stroke at this high frequency was ~5% for 29 MPa applied load. So that the tensile stroke can be more clearly seen, the movie is next shown on 5 times longer time scale.

Movie S3: Real time movie of the electrochemical actuation of a 3-cm-long, coiled CNT@nylon6 sheath-run artificial muscle in 0.2 M TBA·PF₆/PC electrolyte. The applied 0.25 Hz, -3V square-wave inter-electrode voltage produced an actuator stroke of 14.3% for the 36 MPa applied load.

References and Notes

1. M. D. Lima, N. Li, M. Jung de Andrade, S. Fang, J. Oh, G. M. Spinks, M. E. Kozlov, C. S. Haines, D. Suh, J. Foroughi, S. J. Kim, Y. Chen, T. Ware, M. K. Shin, L. D. Machado, A. F. Fonseca, J. D. W. Madden, W. E. Voit, D. S. Galvão, R. H. Baughman, Electrically, chemically, and photonically powered torsional and tensile actuation of hybrid carbon nanotube yarn muscles. *Science* **338**, 928–932 (2012). [doi:10.1126/science.1226762](https://doi.org/10.1126/science.1226762) [Medline](#)
2. X. Gu, Q. Fan, F. Yang, L. Cai, N. Zhang, W. Zhou, W. Zhou, S. Xie, Hydro-actuation of hybrid carbon nanotube yarn muscles. *Nanoscale* **8**, 17881–17886 (2016). [doi:10.1039/C6NR06185K](https://doi.org/10.1039/C6NR06185K) [Medline](#)
3. Y. Sun, Y. Wang, C. Hua, Y. Ge, S. Hou, Y. Shang, A. Cao, Water-responsive helical graphene-oxide fibers incorporating a continuous carbon nanotube network. *Carbon* **132**, 394–400 (2018). [doi:10.1016/j.carbon.2018.02.086](https://doi.org/10.1016/j.carbon.2018.02.086)
4. Y. Song, S. Zhou, K. Jin, J. Qiao, D. Li, C. Xu, D. Hu, J. Di, M. Li, Z. Zhang, Q. Li, Hierarchical carbon nanotube composite yarn muscles. *Nanoscale* **10**, 4077–4084 (2018). [doi:10.1039/C7NR08595H](https://doi.org/10.1039/C7NR08595H) [Medline](#)
5. S. M. Mirvakili, I. W. Hunter, Artificial muscles: Mechanisms, applications, and challenges. *Adv. Mater.* **30**, 1704407 (2018). [doi:10.1002/adma.201704407](https://doi.org/10.1002/adma.201704407) [Medline](#)
6. C. S. Haines, M. D. Lima, N. Li, G. M. Spinks, J. Foroughi, J. D. W. Madden, S. H. Kim, S. Fang, M. Jung de Andrade, F. Göktepe, Ö. Göktepe, S. M. Mirvakili, S. Naficy, X. Lepró, J. Oh, M. E. Kozlov, S. J. Kim, X. Xu, B. J. Swedlove, G. G. Wallace, R. H. Baughman, Artificial muscles from fishing line and sewing thread. *Science* **343**, 868–872 (2014). [doi:10.1126/science.1246906](https://doi.org/10.1126/science.1246906) [Medline](#)
7. S. H. Kim, M. D. Lima, M. E. Kozlov, C. S. Haines, G. M. Spinks, S. Aziz, C. Choi, H. J. Sim, X. Wang, H. Lu, D. Qian, J. D. W. Madden, R. H. Baughman, S. J. Kim, Harvesting temperature fluctuations as electrical energy using torsional and tensile polymer muscles. *Energy Environ. Sci.* **8**, 3336–3344 (2015). [doi:10.1039/C5EE02219C](https://doi.org/10.1039/C5EE02219C)
8. S. Aziz, S. Naficy, J. Foroughi, H. R. Brown, G. M. Spinks, Characterization of torsional actuation in highly twisted yarns and fibres. *Polym. Test.* **46**, 88–97 (2015). [doi:10.1016/j.polymertesting.2015.07.003](https://doi.org/10.1016/j.polymertesting.2015.07.003)
9. P. Zhang, G. Li, Healing-on-demand composites based on polymer artificial muscle. *Polymer (Guildf.)* **64**, 29–38 (2015). [doi:10.1016/j.polymer.2015.03.022](https://doi.org/10.1016/j.polymer.2015.03.022)
10. M. Hiraoka, K. Nakamura, H. Arase, K. Asai, Y. Kaneko, S. W. John, K. Tagashira, A. Omote, Power-efficient low-temperature woven coiled fibre actuator for wearable applications. *Sci. Rep.* **6**, 36358 (2016). [doi:10.1038/srep36358](https://doi.org/10.1038/srep36358) [Medline](#)
11. A. M. Swartz, D. R. Higuera Ruiz, H. P. Feigenbaum, M. W. Shafer, C. C. Browder, Experimental characterization and model predictions for twisted polymer actuators in free torsion. *Smart Mater. Struct.* **27**, 114002 (2018). [doi:10.1088/1361-665X/aad81d](https://doi.org/10.1088/1361-665X/aad81d)
12. H. Cheng, Y. Hu, F. Zhao, Z. Dong, Y. Wang, N. Chen, Z. Zhang, L. Qu, Moisture-activated torsional graphene-fiber motor. *Adv. Mater.* **26**, 2909–2913 (2014). [doi:10.1002/adma.201305708](https://doi.org/10.1002/adma.201305708) [Medline](#)

13. J. Fan, G. Li, High performance and tunable artificial muscle based on two-way shape memory polymer. *RSC Advances* **7**, 1127–1136 (2017). [doi:10.1039/C6RA25024F](https://doi.org/10.1039/C6RA25024F)
14. S. M. Mirvakili, I. W. Hunter, Fast torsional artificial muscles from NiTi twisted yarns. *ACS Appl. Mater. Interfaces* **9**, 16321–16326 (2017). [doi:10.1021/acsami.7b02335](https://doi.org/10.1021/acsami.7b02335) [Medline](#)
15. J. Gong, H. Lin, J. W. C. Dunlop, J. Yuan, Hierarchically arranged helical fiber actuators derived from commercial cloth. *Adv. Mater.* **29**, 1605103 (2017). [doi:10.1002/adma.201605103](https://doi.org/10.1002/adma.201605103) [Medline](#)
16. C. Lamuta, S. Messelot, S. Tawfick, Theory of the tensile actuation of fiber reinforced coiled muscles. *Smart Mater. Struct.* **27**, 055018 (2018). [doi:10.1088/1361-665X/aab52b](https://doi.org/10.1088/1361-665X/aab52b)
17. P. Chen, Y. Xu, S. He, X. Sun, S. Pan, J. Deng, D. Chen, H. Peng, Hierarchically arranged helical fibre actuators driven by solvents and vapours. *Nat. Nanotechnol.* **10**, 1077–1083 (2015). [doi:10.1038/nnano.2015.198](https://doi.org/10.1038/nnano.2015.198) [Medline](#)
18. J. Deng, Y. Xu, S. He, P. Chen, L. Bao, Y. Hu, B. Wang, X. Sun, H. Peng, Preparation of biomimetic hierarchically helical fiber actuators from carbon nanotubes. *Nat. Protoc.* **12**, 1349–1358 (2017). [doi:10.1038/nprot.2017.038](https://doi.org/10.1038/nprot.2017.038) [Medline](#)
19. W. Guo, C. Liu, F. Zhao, X. Sun, Z. Yang, T. Chen, X. Chen, L. Qiu, X. Hu, H. Peng, A novel electromechanical actuation mechanism of a carbon nanotube fiber. *Adv. Mater.* **24**, 5379–5384 (2012). [doi:10.1002/adma.201201845](https://doi.org/10.1002/adma.201201845) [Medline](#)
20. F. Meng, X. Zhang, R. Li, J. Zhao, X. Xuan, X. Wang, J. Zou, Q. Li, Electro-induced mechanical and thermal responses of carbon nanotube fibers. *Adv. Mater.* **26**, 2480–2485 (2014). [doi:10.1002/adma.201305123](https://doi.org/10.1002/adma.201305123) [Medline](#)
21. I. Agnarsson, A. Dhinojwala, V. Sahni, T. A. Blackledge, Spider silk as a novel high performance biomimetic muscle driven by humidity. *J. Exp. Biol.* **212**, 1990–1994 (2009). [doi:10.1242/jeb.028282](https://doi.org/10.1242/jeb.028282) [Medline](#)
22. J. Foroughi, G. M. Spinks, G. G. Wallace, J. Oh, M. E. Kozlov, S. Fang, T. Mirfakhrai, J. D. W. Madden, M. K. Shin, S. J. Kim, R. H. Baughman, Torsional carbon nanotube artificial muscles. *Science* **334**, 494–497 (2011). [doi:10.1126/science.1211220](https://doi.org/10.1126/science.1211220) [Medline](#)
23. J. A. Lee, N. Li, C. S. Haines, K. J. Kim, X. Lepró, R. Ovalle-Robles, S. J. Kim, R. H. Baughman, Electrochemically powered, energy-conserving carbon nanotube artificial muscles. *Adv. Mater.* **29**, 1700870 (2017). [doi:10.1002/adma.201700870](https://doi.org/10.1002/adma.201700870) [Medline](#)
24. S. H. Kim, C. H. Kwon, K. Park, T. J. Mun, X. Lepró, R. H. Baughman, G. M. Spinks, S. J. Kim, Bio-inspired, moisture-powered hybrid carbon nanotube yarn muscles. *Sci. Rep.* **6**, 23016 (2016). [doi:10.1038/srep23016](https://doi.org/10.1038/srep23016) [Medline](#)
25. M. D. Lima, S. Fang, X. Lepró, C. Lewis, R. Ovalle-Robles, J. Carretero-González, E. Castillo-Martínez, M. E. Kozlov, J. Oh, N. Rawat, C. S. Haines, M. H. Haque, V. Aare, S. Stoughton, A. A. Zakhidov, R. H. Baughman, Biscrolling nanotube sheets and functional guests into yarns. *Science* **331**, 51–55 (2011). [doi:10.1126/science.1195912](https://doi.org/10.1126/science.1195912) [Medline](#)
26. Materials and methods are available as supplementary materials.

27. S. H. Kim, C. S. Haines, N. Li, K. J. Kim, T. J. Mun, C. Choi, J. Di, Y. J. Oh, J. P. Oviedo, J. Bykova, S. Fang, N. Jiang, Z. Liu, R. Wang, P. Kumar, R. Qiao, S. Priya, K. Cho, M. Kim, M. S. Lucas, L. F. Drummy, B. Maruyama, D. Y. Lee, X. Lepró, E. Gao, D. Albarq, R. Ovalle-Robles, S. J. Kim, R. H. Baughman, Harvesting electrical energy from carbon nanotube yarn twist. *Science* **357**, 773–778 (2017). [doi:10.1126/science.aam8771](https://doi.org/10.1126/science.aam8771) [Medline](#)
28. M. Ue, A. Murakami, S. Nakamura, A convenient method to estimate ion size for electrolyte materials design. *J. Electrochem. Soc.* **149**, A1385–A1388 (2002). [doi:10.1149/1.1507593](https://doi.org/10.1149/1.1507593)
29. M. A. McEvoy, N. Correll, Materials science. Materials that couple sensing, actuation, computation, and communication. *Science* **347**, 1261689 (2015). [doi:10.1126/science.1261689](https://doi.org/10.1126/science.1261689) [Medline](#)
30. T. Miyata, N. Asami, T. Urugami, A reversibly antigen-responsive hydrogel. *Nature* **399**, 766–769 (1999). [doi:10.1038/21619](https://doi.org/10.1038/21619) [Medline](#)
31. J. Lee, S. Ko, C. H. Kwon, M. D. Lima, R. H. Baughman, S. J. Kim, Carbon nanotube yarn-based glucose sensing artificial muscle. *Small* **12**, 2085–2091 (2016). [doi:10.1002/sml.201503509](https://doi.org/10.1002/sml.201503509) [Medline](#)
32. T. Wang, S. Kumar, Electrospinning of polyacrylonitrile nanofibers. *J. Appl. Polym. Sci.* **102**, 1023–1029 (2006). [doi:10.1002/app.24123](https://doi.org/10.1002/app.24123)
33. K. Takashima, J. Rossiter, T. Mukai, McKibben artificial muscle using shape-memory polymer. *Sens. Actuators A Phys.* **164**, 116–124 (2010). [doi:10.1016/j.sna.2010.09.010](https://doi.org/10.1016/j.sna.2010.09.010)
34. S. Aziz, S. Naficy, J. Foroughi, H. R. Brown, G. M. Spinks, Controlled and scalable torsional actuation of twisted nylon 6 fiber. *J. Polym. Sci. B* **54**, 1278–1286 (2016). [doi:10.1002/polb.24035](https://doi.org/10.1002/polb.24035)
35. R. G. Budynas, J. K. Nisbett, *Shigley's Mechanical Engineering Design* (McGraw-Hill, 2008), pp.116–117.
36. C. S. Haines, N. Li, G. M. Spinks, A. E. Aliev, J. Di, R. H. Baughman, New twist on artificial muscles. *Proc. Natl. Acad. Sci. U.S.A.* **113**, 11709–11716 (2016). [doi:10.1073/pnas.1605273113](https://doi.org/10.1073/pnas.1605273113) [Medline](#)
37. M. Elsherif, M. U. Hassan, A. K. Yetisen, H. Butt, Glucose sensing with phenylboronic acid functionalized hydrogel-based optical diffusers. *ACS Nano* **12**, 2283–2291 (2018). [doi:10.1021/acsnano.7b07082](https://doi.org/10.1021/acsnano.7b07082) [Medline](#)